Journal of Theoretical Biology 596 (2025) 111977

Contents lists available at ScienceDirect

Journal of Theoretical Biology

journal homepage: www.elsevier.com/locate/yjtbi

Implementation of actin polymerization and depolymerization in a two-dimensional cell migration model and its implications on mammalian cell morphology and velocity

Lingxing Yao [a], Yizeng Li [b,*]

[a] Department of Mathematics, University of Akron, Akron, OH 44325, USA
[b] Department of Biomedical Engineering, Binghamton University, SUNY, Binghamton, NY 13902, USA

A B S T R A C T

Cell migration, a pivotal process in wound healing, immune response, and even cancer metastasis, manifests through intricate interplay between morphology, speed, and cytoskeletal dynamics. Mathematical modeling emerges as a powerful tool to dissect these complex interactions. This work presents a two-dimensional immersed boundary model for mammalian cell migration, incorporating both filamentous actin (F-actin) and monomeric actin (G-actin) to explicitly capture polymerization and depolymerization. This model builds upon our previous one-dimensional efforts, now enabling us to explore the impact of G-actin on not just cell velocity but also morphology. We compare predictions from both models, revealing that while the one-dimensional model captures core dynamics along the cell's axis, the two-dimensional model excels in portraying cell shape evolution and transverse variations in actin concentration and velocity. Our findings highlight the crucial role of including G-actin in shaping cell morphology. Actin velocity aligned with migration direction elongates the cell, while velocity normal to the membrane promotes spreading. Importantly, the model establishes a link between these microscopic aspects and macroscopic observables like cell shape, offering a deeper understanding of cell migration dynamics. This work not only provides a more comprehensive picture of cell migration but also paves the way for future studies exploring the interplay of actin dynamics, cell morphology, and biophysical parameters in diverse biological contexts.

1. Introduction

Cell migration plays a pivotal role in diverse biological processes such as wound healing, immune response, and cancer metastasis (van der Woude et al., 2017; Baeyens and Schwab, 2020; Jorgensen and Sanders, 2016; Montell et al., 2012). This dynamic phenomenon manifests through multiple observable features, encompassing morphology, speed, polarization, and directionality (Pollard and Cooper, 2009; Keren et al., 2008; Kozlov and Mogilner, 2007). These characteristics are influenced by a multitude of factors, including extracellular matrix properties, intracellular actin dynamics, fluid flows within and outside the cell, and the biochemical molecular environments (Keren et al., 2009; Inagaki and Katsuno, 2017; Rappel and Edelstein-Keshet, 2017; Alert and Trepat, 2020; Blackley et al., 2021; Maity et al., 2022; Bera et al., 2022). Mathematical modeling emerges as a powerful tool capable of providing unique insights and quantifications into the diverse features of cell migration.

Physiology-informed, continuum mechanics-based models formulated as partial differential equations are potent due to their ability to capture cell dynamics with high spatial and temporal resolution. Such models also face challenges with moving boundaries, a necessary process for studying cell migration. One of the mature moving boundary techniques is the immersed boundary method (Peskin, 2002), a versatile tool in computational fluid dynamics for modeling fluids interacting with complex, moving objects such as mammalian cell membranes (Mittal and Iaccarino, 2005; Kim et al., 2012). This method is particularly powerful in handling fluid flow across the moving boundary. These useful features enable an advanced two-phase cell migration study where cytosol and actin network are equally treated (Dembo and Harlow, 1986; Li and Sun, 2018; Li et al., 2019). The main component of the actin network is the filamentous actin (F-actin). While a single actin filament behaves like an elastic object, the F-actin network at large time scale (on the order of minutes or longer) is dynamic and mobile, lacking a stable reference configuration. Consequently, within the two-phase framework, the actin network is treated as a fluid-like material.

In the past, we have developed an immersed boundary-based two-phase cell migration model, which demonstrated success and promises in studying the interplay between cytosol and F-actin network (Li et al., 2019; Yao and Li, 2022). In the model, we strategically transformed the conservation of mass and momentum equations of the actin network into one effective diffusion-reaction-advection equation for the actin phase, allowing the actin network dynamics to be computed through time evolution processes. In addition, the model featured osmosis and passive and active solute transport across the cell membrane. The

* Corresponding author.
E-mail address: yli33@binghamton.edu (Y. Li).

https://doi.org/10.1016/j.jtbi.2024.111977
Received 13 March 2024; Received in revised form 15 October 2024; Accepted 21 October 2024
Available online 5 November 2024

interaction between intracellular and extracellular flow fields makes it possible to quantify cytosol dynamics under the influence of membrane solute channels and pumps. The coupling of fluid–structure interaction and osmosis established innovative techniques in the mathematical modeling of mammalian cell migration.

In this work, moving beyond our previous endeavors (Li et al., 2019; Yao and Li, 2022), we will incorporate monomeric actin (G-actin) into the two-dimensional immersed-boundary framework to explicitly model actin polymerization and depolymerization between F-actin and G-actin (Pollard and Borisy, 2003; Lomakin et al., 2015). The G-actin possesses its own diffusion-reaction-advection equation, adding another layer of biophysics versatility that allows us to capture the crucial role of G-actin in cell polarization and morphological changes. To resolve the computational challenges with a two-dimensional model, we will employ an implicit method for fluid–structure interaction to enhance stability and accuracy for complex geometries and dynamics. This enables us to study a broader range of biophysical parameters and delve deeper into the processes of cell migration as opposed to the explicit method we used previously.

In our earlier studies, our cell migration models incorporated G-actin but were constrained to one-dimensional models where all quantities varied solely along the x-direction (Yao and Li, 2022; Yao et al., 2023; Li and Sun, 2024). Consequently, we were not able to capture cell morphology and the underlying mechanisms driving it. The adoption of a two-dimensional model now allows us to explore how G-actin influences not only cell migration velocity but also the actual morphology of the cell, providing a more comprehensive understanding of its role in cell movement. By directly comparing predictions from the one-dimensional and two-dimensional models, we can dissect the impact of dimensionality on cell behavior and gain profound insights into how different actin dynamics influence *in vivo* cell migration. The primary objective of this study is to quantify the impact of actin polymerization and depolymerization in a two-dimensional space and compare the similarities and differences between the results obtained from the two models.

This paper is organized as follows. We begin with a description of the full multi-modular biophysical model that includes cytosol, extracellular fluid, F-actin, G-actin, and the coupling among these components, followed by detailed numerical methods for this model. We then present features of model predictions on cell morphology, polarization, and velocity under different actin conditions, with insights into the comparison between predictions from a one-dimensional model versus a two-dimensional one. In contrast to our earlier two-dimensional models (Yao and Mori, 2017; Li et al., 2019; Yao and Li, 2022), this study exclusively concentrates on actin-driven cell migration and therefore omits consideration of a solute module. This means we do not account for osmosis-induced water flux and water-driven cell migration. Nevertheless, the cytosol and extracellular fluid fields remain essential to maintain the integrity of the fluid–structure interaction inherent in cell motility.

2. The biophysical model

Here we present the complete biophysical model employed in this study. The two-dimensional cell model is defined within a rectangular domain $\Omega \subset \mathbb{R}^2$, partitioned into intracellular space Ω_{I} and extracellular space Ω_{E} by a closed membrane Γ ($\Omega = \Omega_{\mathrm{I}} \cup \Gamma \cup \Omega_{\mathrm{E}}$). The material coordinates for the membrane are denoted by $s \in [0, 2\pi)$. The membrane's evolution is described by $\boldsymbol{X}(s,t) \in \Omega$, where the contour traced by $\boldsymbol{X}(s,t)$ characterizes the shape of the membrane Γ. F-actin (concentration θ_{n}) and G-actin (concentration θ_{c}) are confined within Ω_{I}, while the water spans the entire domain Ω; this treatment allows water to permeate the cell membrane. Intracellular water represents the cytosol, whereas extracellular water represents the extracellular fluid. The water is modeled as a Newtonian, incompressible flow with viscosity μ, with velocity $\boldsymbol{v}_{\mathrm{c}}$ and pressure p. The dynamic variables of interest in the model encompass $\boldsymbol{X}$, θ_{n}, θ_{c}, $\boldsymbol{v}_{\mathrm{c}}$, p, and the F-actin velocity $\boldsymbol{v}_{\mathrm{n}}$.

2.1. Cytosol

The conservation of momentum for the cytosol phase is

$$\nabla \cdot \Sigma_{\mathrm{m}}(\boldsymbol{v}_{\mathrm{c}}, p) - \eta\theta_{\mathrm{n}}(\boldsymbol{v}_{\mathrm{c}} - \boldsymbol{v}_{\mathrm{n}}) = 0, \quad \nabla \cdot \boldsymbol{v}_{\mathrm{c}} = 0, \tag{1}$$

where $\boldsymbol{v}_{\mathrm{c}}$ and p are the velocity and pressure of the fluid, respectively. $\boldsymbol{v}_{\mathrm{n}}$ and θ_{n} are the velocity and concentration of the F-actin network, respectively. Since the actin network is only defined within the cell domain, $\boldsymbol{v}_{\mathrm{n}}$ and θ_{n} are both zero when calculating the extracellular fluid in Ω_{E}. η is the interfacial stress coefficient between the cytosol and the F-actin network (Li and Sun, 2018; Li et al., 2019). The two velocities, $\boldsymbol{v}_{\mathrm{c}}$ and $\boldsymbol{v}_{\mathrm{n}}$, are the macro-scale average velocities. The interfacial stress, $\eta\theta_{\mathrm{n}}(\boldsymbol{v}_{\mathrm{c}} - \boldsymbol{v}_{\mathrm{n}})$, arises when the cytosol and the F-actin network have different velocities, and is proportional to the amount of F-actin that is present.[1] In (1),

$$\Sigma_{\mathrm{m}}(\boldsymbol{v}_{\mathrm{c}}, p) = \mu\left(\nabla\boldsymbol{v}_{\mathrm{c}} + (\nabla\boldsymbol{v}_{\mathrm{c}})^{\mathrm{T}}\right) - p\mathbf{I}, \tag{2}$$

is the stress in the cytosol phase due to the combined effect of the fluid pressure and viscous shear stress. $\mathbf{I}$ is an identity matrix. We have disregarded forces acting on the cytosol aside from hydrostatic pressure, viscous shear stress, and interfacial stress.

2.2. Actin kinematics

The kinematics of F-actin and G-actin within the cell, Ω_{I}, are coupled through polymerization and depolymerization. The governing equation for F-actin is

$$\frac{\partial\theta_{\mathrm{n}}}{\partial t} + \nabla \cdot (\boldsymbol{v}_{\mathrm{n}}\theta_{\mathrm{n}}) = -\gamma\theta_{\mathrm{n}} \tag{3}$$

where γ is the rate of actin depolymerization. The kinematic boundary condition for F-actin on the cell membrane, Γ_{i}, is Li and Sun (2018), Li et al. (2019)

$$\theta_{\mathrm{n}}\left(\boldsymbol{v}_{\mathrm{n}} - \frac{\partial\boldsymbol{X}}{\partial t}\right) \cdot \mathbf{n} = J_{\mathrm{actin}}, \tag{4}$$

where $\mathbf{n}$ is the outward norm of Γ. J_{actin} is the F-actin flux, coming from actin polymerization that typically happens at the cell boundary. This boundary condition suggests that the F-actin flux resulting from polymerization will either create an inward velocity known as actin retrograde flow, contribute to the movement of the cell membrane, or both. The rate of actin polymerization depends on the availability of G-actin. Therefore, we model this flux in the form (Yao et al., 2023)

$$J_{\mathrm{actin}} = j(s)\frac{\theta_{\mathrm{c}}}{\theta_{\mathrm{c}} + \theta_0}, \tag{5}$$

where $j(s)$ is the strength of the actin flux, in which s is the material coordinate along the membrane. We assume that $j(s)$ is polarized as a result of signaling effects that are beyond the scope of this study. θ_{c} is the concentration of G-actin, and θ_0 is a constant that modulates the amplitude of the actin flux.

The governing equation for G-actin is

$$\frac{\partial\theta_{\mathrm{c}}}{\partial t} + \nabla \cdot (\boldsymbol{v}_{\mathrm{c}}\theta_{\mathrm{c}}) = D_{\mathrm{c}}\nabla^2\theta_{\mathrm{c}} + \gamma\theta_{\mathrm{n}}, \tag{6}$$

where D_{c} is the diffusion coefficient of G-actin in the cytosol. The corresponding kinematic boundary condition is

$$(\boldsymbol{v}_{\mathrm{c}}\theta_{\mathrm{c}} - D_{\mathrm{c}}\nabla\theta_{\mathrm{c}}) \cdot \mathbf{n} = \theta_{\mathrm{c}}\frac{\partial\boldsymbol{X}}{\partial t} \cdot \mathbf{n} - J_{\mathrm{actin}}. \tag{7}$$

This boundary condition suggests that the consumption of G-actin through actin polymerization is balanced by both the total flux of G-actin and the movement of the membrane.

[1] At the microscale, the no-slip condition applies at the interface. However, when the average velocities of the actin and cytosol differ, boundary layers and velocity gradients form near the interface. These gradients create viscous shear stress, leading to interfacial stress that allows momentum to transfer across the interface. In our model, we treat this interfacial stress macroscopically, making it an effective body forces acting on the cytosol and actin network.

2.3. Actin kinetics

The conservation of momentum for the F-actin network is

$$-\nabla\sigma + \eta\theta_{\mathrm{n}}(\boldsymbol{v}_{\mathrm{c}} - \boldsymbol{v}_{\mathrm{n}}) - \eta_{\mathrm{st}}\theta_{\mathrm{n}}\boldsymbol{v}_{\mathrm{n}} = 0, \tag{8}$$

where η_{st} is the strength of focal adhesion (Li and Sun, 2018; Li et al., 2019). The term $\eta_{\mathrm{st}}\theta_{\mathrm{n}}\boldsymbol{v}_{\mathrm{n}}$ represents the effective body force from the substrate to the F-actin network. σ is the magnitude of the isotropic stress within the F-actin network. In this model, we use a linear constitutive relation for this stress

$$\sigma = k_{\sigma_{\mathrm{n}}}\theta_{\mathrm{n}}, \tag{9}$$

where $k_{\sigma_{\mathrm{n}}}$ is the coefficient of F-actin stress. We neglect the viscous shear stress in the F-actin network because it is less significant compared to the stress from focal adhesion (based on the value of η_{st} and the effective viscosity of actin network (Stricker et al., 2010)).

Given this constitutive condition, we can express the term $\theta_{\mathrm{n}}\boldsymbol{v}_{\mathrm{n}}$ in (8) as

$$\theta_{\mathrm{n}}\boldsymbol{v}_{\mathrm{n}} = \frac{\eta\theta_{\mathrm{n}}\boldsymbol{v}_{\mathrm{c}}}{\eta+\eta_{\mathrm{st}}} - \frac{k_{\sigma_{\mathrm{n}}}}{\eta+\eta_{\mathrm{st}}}\nabla\theta_{\mathrm{n}}. \tag{10}$$

With this relation, we can convert (3) to an effective diffusion-advection-reaction equation for the F-actin network in the form (Li et al., 2019; Yao et al., 2023)

$$\frac{\partial\theta_{\mathrm{n}}}{\partial t} + \nabla\cdot\left(\frac{\eta\boldsymbol{v}_{\mathrm{c}}}{\eta+\eta_{\mathrm{st}}}\theta_{\mathrm{n}}\right) = \frac{k_{\sigma_{\mathrm{n}}}}{\eta+\eta_{\mathrm{st}}}\nabla^2\theta_{\mathrm{n}} - \gamma\theta_{\mathrm{n}}. \tag{11}$$

The term $k_{\sigma_{\mathrm{n}}}/(\eta+\eta_{\mathrm{st}})$, which is a ratio of F-actin relaxation to the actin-matrix interaction (Yao et al., 2023), is the effective diffusion coefficient of the F-actin network. Eq. (11) has the form that can be directly implemented into our computational framework (Li et al., 2019). The boundary condition (4) becomes

$$\theta_{\mathrm{n}}\frac{\eta}{\eta+\eta_{\mathrm{st}}}\boldsymbol{v}_{\mathrm{c}}\cdot\mathbf{n} + \frac{k_{\sigma_{\mathrm{n}}}}{\eta+\eta_{\mathrm{st}}}\nabla\theta_{\mathrm{n}}\cdot\mathbf{n} = \theta_{\mathrm{n}}\frac{\partial\boldsymbol{X}}{\partial t}\cdot\mathbf{n} + J_{\mathrm{actin}}. \tag{12}$$

2.4. Membrane

A key feature of the immersed boundary model is the force transfer between the structure, which is the cell membrane in this model, and the fluid. We use a linear constitutive relation for the cell membrane in the form (Peskin, 2002)

$$\boldsymbol{F}_{\mathrm{mem}} = \frac{\partial}{\partial s}(T\boldsymbol{\tau}), \quad T = k_m\left(\left|\frac{\partial\boldsymbol{X}}{\partial s}\right| - 1\right), \tag{13}$$

where $\boldsymbol{\tau}$ is the unit tangent direction along the membrane Γ, k_m is the coefficient of membrane stress, and $|\partial\boldsymbol{X}/\partial s|$ is the Jacobian determinant, describing the length change of the membrane. $T\boldsymbol{\tau}$ is the membrane tension along the tangential direction. Differentiating this tangential tension along the arc length gives a tension normal to the membrane, $\boldsymbol{F}_{\mathrm{mem}}$.

The membrane velocity, $\partial\boldsymbol{X}/\partial t$, is determined by both the cytosol velocity and the water flux, j_{w}, across the membrane (Kim and Peskin, 2006; Li et al., 2017; Li and Sun, 2018; Li et al., 2019; Yao and Li, 2022),

$$\frac{\partial\boldsymbol{X}}{\partial t} = \boldsymbol{v}_{\mathrm{c}} - j_{\mathrm{w}}\mathbf{n}, \quad j_{\mathrm{w}} = k_{\mathrm{w}}[\psi], \quad \psi = -\mathbf{n}\cdot(\Sigma_{\mathrm{m}}(\boldsymbol{v}_{\mathrm{c}}, p))\mathbf{n}, \tag{14}$$

where the square brackets indicate the jump in values on the two sides of the interface, $\mathbf{n}$ is the outward normal along Γ, and k_{w} is membrane water permeability. Eq. (14) is a modified non-slip boundary condition to account for water flux across the cell membrane.

The difference in the fluid stress on the two sides of the membrane is balanced by all the other forces acting on the membrane. The force balance of the cell membrane is given by

$$\left[\Sigma_{\mathrm{m}}(\boldsymbol{v}_{\mathrm{c}}, p)\mathbf{n}\right] = \sigma\mathbf{n} + \boldsymbol{F}_{\mathrm{mem}}\left|\frac{\partial\boldsymbol{X}}{\partial s}\right|^{-1} + \boldsymbol{F}_{\mathrm{ad}}, \tag{15}$$

where $\boldsymbol{F}_{\mathrm{ad}}$ is the resistance force from the cell membrane (Yao et al., 2023). This force represents a generic resistance from the attachment of the cell membrane to the substrate, and is different from the force of focal adhesion defined throughout the cell (see Eq. (8)). We let this resistance force be proportional to the membrane velocity in the form

$$\boldsymbol{F}_{\mathrm{ad}} = -k_{\mathrm{ad}}\frac{\partial\boldsymbol{X}}{\partial t}, \tag{16}$$

where k_{ad} is the coefficient of the resistance force.

2.5. Fluid–structure interaction

In the standard immersed boundary (IB) form, the fluid momentum balance in (1) and the interface force balance condition in (15) can be formulated in the form

$$\begin{aligned}&\boldsymbol{f}(\boldsymbol{x},t) + \nabla\cdot\Sigma_{\mathrm{m}}(\boldsymbol{v}_{\mathrm{c}}, p) - \eta\theta_{\mathrm{n}}(\boldsymbol{v}_{\mathrm{c}} - \boldsymbol{v}_{\mathrm{n}}) = 0,\\ &\boldsymbol{f}(\boldsymbol{x},t) = \int_{\Gamma}\left((\sigma\mathbf{n} + \boldsymbol{F}_{\mathrm{ad}})\left|\frac{\partial\boldsymbol{X}}{\partial s}\right| + \boldsymbol{F}_{\mathrm{mem}}\right)\delta(\boldsymbol{x} - \boldsymbol{X}(s,t))ds,\end{aligned} \tag{17}$$

where δ is a two-dimensional Dirac delta function. The incompressible condition for the cytosol velocity $\boldsymbol{v}_{\mathrm{c}}$ remains unchanged in the IB form

$$\nabla\cdot\boldsymbol{v}_{\mathrm{c}} = 0. \tag{18}$$

The membrane velocity in (14) can be rewritten by the interface force balance in (15) as

$$\boldsymbol{v}_{\mathrm{c}} - \frac{\partial\boldsymbol{X}}{\partial t} = -k_{\mathrm{w}}\left[\sigma + \left(\boldsymbol{F}_{\mathrm{ad}} + \boldsymbol{F}_{\mathrm{mem}}\left|\frac{\partial\boldsymbol{X}}{\partial s}\right|^{-1}\right)\cdot\mathbf{n}\right]\mathbf{n}. \tag{19}$$

Now our model includes (17), (18), (11), and (6), with boundary conditions (19), (12), and (7).

3. Numerical algorithm

In this Numerical Algorithm section, a "cell" refers to a rectangular spatial discretization unit. This term should not be confused with the mammalian cell occupying the domain Ω_{I}. This convention only applies within this Numerical Algorithm section.

The numerical scheme operates over the computational domain $\Omega = [0, L] \times [0, L]$. Here, we establish a fixed Cartesian grid with vertices located at (x_i, y_j), where $x_i = i\Delta x$ for $i = 0, \ldots, N$, and $y_j = j\Delta y$ for $j = 0, \ldots, N$. The centers of the grid cells are denoted by $(x_{i+1/2}, y_{j+1/2})$. Within each $\Delta x \times \Delta y$ cell, the F-actin concentration (θ_{n}), G-actin concentration (θ_{c}), and fluid pressure (p) are defined at cell centers. The fluid velocity $\boldsymbol{v}_{\mathrm{c}} = (u, v)$ is assigned to the vertical and horizontal edges, respectively, based on the MAC (marker and cell) grid arrangement. Throughout the discussion, we assume $h = \Delta y = \Delta y$. Additionally, we adopt a uniform discretization for the membrane, Γ, on the reference interface Γ_{ref}. The immersed boundary (IB) points are represented by $\boldsymbol{X}(s_i, t)$, where $i = 1, \ldots, N_\Gamma$ and $s_i = (i-1)\Delta s$. At each step, we construct a cubic spline parametric representation of the immersed boundary.

The cell centers can be classified based on their positional relationship with the IB. *Regular grid centers* do not have neighboring cell centers on the opposite side of the membrane, Γ; for example, points p_5 and p_7 in Fig. 1(A). *Irregular grid centers* have at least one neighboring cell center situated on the other side of Γ, such as points A and B in Fig. 1(A). Discretization of the F-actin and G-actin Eqs. (6) and (11) depends on whether the cell center is regular or irregular. To enforce the actin boundary condition at Γ, we introduce auxiliary variables for θ_{n} and θ_{c}. These variables are defined at *grid crossings*, the points where the immersed boundary Γ intersects the grid lines connecting cell centers. At each of these grid crossings, two auxiliary variables, $\theta_{\mathrm{n}}^{\mathrm{b}}$ and $\theta_{\mathrm{c}}^{\mathrm{b}}$, are defined, representing the values of the actin at the Ω_{I} face of the membrane. These $\theta_{\mathrm{n}}^{\mathrm{b}}$ and $\theta_{\mathrm{c}}^{\mathrm{b}}$ variables are employed to discretize the boundary conditions (4) and (7), along with Eqs. (6) and (11) at irregular centers.

The overall algorithm follows this outline: for each time step, we alternate between the fluid–structure interaction (FSI) substep and the

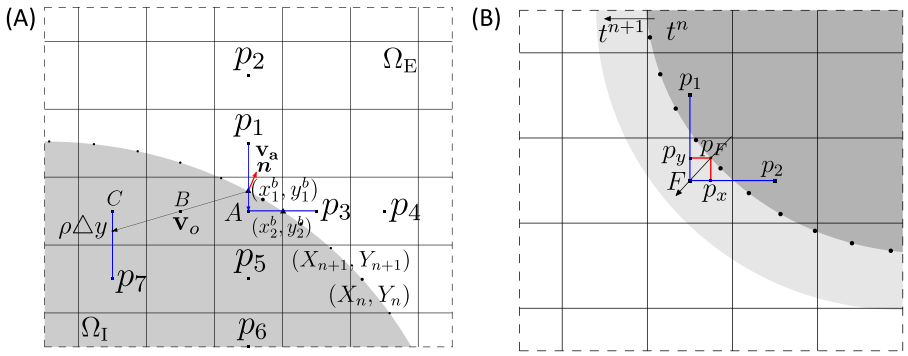

Fig. 1. Schematics of numerical strategies. (A) Extrapolation scheme for actin concentration. (B) Treatment of freshly cleared grid.

actin substep, which is further divided into F-actin and G-actin components. At a given time step, we have the values $u^n, v^n, p^n, \boldsymbol{X}^n, \theta_n^n, \theta_c^n, \theta_n^{b,n}$, $\theta_c^{b,n}$, where the superscript n represents the values of the grid variables at time $t = n\Delta t$ with $n = 0, 1, \ldots$, and Δt is the time step.

Substep 1 With u^n, v^n, p^n, and $\boldsymbol{X}^n$ as inputs, we employ an implicit IB method (Mori et al., 2008) to calculate u^{n+1}, v^{n+1}, p^{n+1}, and $\boldsymbol{X}^{n+1}$ based on Eqs. (17) and (18), subject to the condition (19). The determination of F-actin at IB locations, denoted as $\theta_n^{IB,n}$, is crucial for Eqs. (17) and (19). This quantity is derived through interpolation from the concentration values $\theta_n^{b,n}$ defined at grid crossings.

Substep 2 Given the updated IB point locations $\boldsymbol{X}^{n+1}$ and the fluid velocity (u^{n+1}, v^{n+1}), solve the moving boundary advection-diffusion problem for G-actin concentration (θ_c^{n+1} and $\theta^{b,n+1}$) and F-actin problem concentration (θ_n^{n+1} and $\theta_n^{b,n+1}$). Special attention is required in the discretization of Eqs. (6) and (11) at irregular grid centers. This is particularly crucial for *freshly cleared centers*, referring to computational cell centers that were situated in Ω_E in the previous time step but are now within Ω_I. The enforcement of boundary conditions (7) and (11) is facilitated at grid crossings through the utilization of auxiliary concentration variables defined at those points.

3.1. Implicit IB method for fluid velocity and IB locations

Given the values of $\boldsymbol{v}_c^n$, p^n, $\boldsymbol{X}^n$, and $\theta_n^{b,n}$, the initial step of the update scheme involves the simultaneous solution of (17), (18), and (19).

For the computation of the membrane force $\boldsymbol{F}_{mem}$ in (13), we introduce differencing operators acting on functions W defined on the IB grid ($k = 1, \ldots, N_\Gamma$): $D_s^{\pm} W_k = \pm(W_{k\pm1} - W_k)/\Delta s$. Using these operators, we discretize (13) in the form

$$\boldsymbol{F}_{mem,k}^n = k_m D_s^+ \left(-\left| D_s^- \boldsymbol{X}_k^n \right|^{-1} D_s^- \boldsymbol{X}_k^n \right), \tag{20}$$

where the differencing operators above act component-wise.

The fully time-implicit IB treatment ($s_\alpha^{\bar{n}} = |\partial \bar{\boldsymbol{X}}^n / \partial s|$) of the FSI is given by

$$0 = G_h \cdot \bar{\boldsymbol{v}}_c, \tag{21}$$

$$0 = -G_h \bar{p} + \mu L_h \bar{\boldsymbol{v}}_c + \eta \theta_n (\boldsymbol{v}_n^n - \boldsymbol{v}_c^n) + S_{\bar{h}} \left((\sigma^n \mathbf{n} + \boldsymbol{F}_{ad}^{n+1}) s_\alpha^{\bar{n}} + \bar{\boldsymbol{F}}_{mem} \right), \tag{22}$$

and

$$\frac{\boldsymbol{X}^{n+1} - \boldsymbol{X}^n}{\Delta t} = S_{\bar{h}}^* \bar{\boldsymbol{v}}_c + k_w \left(\sigma^n + \boldsymbol{F}_{ad}^{n+1} \cdot \mathbf{n} + \frac{1}{s_\alpha^{\bar{n}}} \bar{\boldsymbol{F}}_{mem} \mathbf{n} \right) \mathbf{n}. \tag{23}$$

In this IB formulation, G_h, $G_h \cdot$, and L_h correspond to suitable discretization of the gradient, divergence, and Laplacian operators, respectively. σ^n is the F-actin network stress from previous step ($\sigma^n = k_{\sigma_n} \theta_n^n$). The midpoint values are $\bar{\boldsymbol{v}}_c = (\boldsymbol{v}_c^{n+1} + \boldsymbol{v}_c^n)/2$, $\bar{\boldsymbol{X}} = (\boldsymbol{X}^{n+1} + \boldsymbol{X}^n)/2$, and $\bar{\boldsymbol{F}}_{mem} = \boldsymbol{F}_{mem}(\bar{\boldsymbol{X}})$. Additionally, $\boldsymbol{F}_{ad}^{n+1} = k_{ad}(\boldsymbol{X}^{n+1} - \boldsymbol{X}^n)/\Delta t$. The operators $S_{\bar{h}}$ and $S_{\bar{h}}^*$ indicate that spreading and interpolation are performed on $\bar{\boldsymbol{X}}$.

The spreading operator S_h in (22) is utilized for the discretization of the Eulerian function $\boldsymbol{f}$ in (17), which is defined on the MAC grid. For instance, if we intend to spread $\boldsymbol{F}_{mem}^n = (F_x^n, F_y^n)$ at all IB point positions $\boldsymbol{X}^n = (X^n, Y^n)$ to $\boldsymbol{f}^n = (f^n, g^n)$, the following two conditions need to be met.

$$\begin{aligned} f_{i,j+\frac{1}{2}}^n &= \sum_{k=1}^{N_\Gamma} F_{x,k}^n \delta_h(x_i - X_k^n) \delta_h(y_{j+\frac{1}{2}} - Y_k^n) \Delta s, \\ g_{i+\frac{1}{2},j}^n &= \sum_{k=1}^{N_\Gamma} F_{y,k}^n \delta_h(x_{i+\frac{1}{2}} - X_k^n) \delta_h(y_j - Y_k^n) \Delta s, \end{aligned} \tag{24}$$

where $\delta_h(r)$ is a regularized discrete delta function. In this work, we use the discrete delta function in the form (Peskin, 2002)

$$\begin{aligned} \delta_h(r) &= \frac{1}{h} \phi\left(\frac{r}{h}\right), \\ \phi(r) &= \begin{cases} \frac{1}{8}(3 - 2|r| + \sqrt{1 + 4|r| - 4r^2}) & |r| \le 1, \\ \frac{1}{8}(5 - 2|r| - \sqrt{-7 + 12|r| - 4r^2}) & 1 < |r| \le 2, \\ 0 & 2 < |r|. \end{cases} \end{aligned} \tag{25}$$

Similarly, if we need to interpolate $\boldsymbol{v}_c^n = (u^n, v^n)$ on the MAC grid to the kth IB point velocity $\boldsymbol{U}_k^n = (U_k^n, V_k^n)$ using interpolation operator S_h^*, as in (23), we need

$$\begin{aligned} U_k^n &= \sum_{i,j} u_{i,j+\frac{1}{2}}^n \delta_h(x_i - X_k^n) \delta_h(y_{j+\frac{1}{2}} - Y_k^n) h^2, \\ V_k^n &= \sum_{i,j} v_{i+\frac{1}{2},j}^n \delta_h(x_{i+\frac{1}{2}} - X_k^n) \delta_h(y_j - Y_k^n) h^2. \end{aligned} \tag{26}$$

An iterative scheme is needed to compute (21)–(22). We use superscript ^{k} to indicate the kth iteration, and the iterative variables are $\boldsymbol{v}_c^{\bar{n},k} = (\boldsymbol{v}_c^n + \boldsymbol{v}_c^{n,k})/2$, and $(\boldsymbol{X}^n + \boldsymbol{X}^{n,k})/2 = \boldsymbol{X}^{\bar{n},k}$. Therefore, we have

$$G_h \cdot \boldsymbol{v}_c^{\bar{n},k+1} = 0, \tag{27}$$

$$\begin{aligned} 0 = &- G_h \bar{p}^{n,k+1} + \mu L_h \boldsymbol{v}_c^{\bar{n},k+1} + \eta \theta_n (\boldsymbol{v}_n^n - \boldsymbol{v}_c^{\bar{n},k}) \\ &+ S_{\bar{n},k} \left(\sigma^n s_\alpha^{\bar{n},k} \mathbf{n} - k_{ad} s_\alpha^{\bar{n},k} \mathbf{n}\mathbf{n}^T \frac{\boldsymbol{X}^{n,k+1} - \boldsymbol{X}^n}{\Delta t} + \boldsymbol{F}_{mem}^{\bar{n},k} + J_{\bar{n},k} (\boldsymbol{X}^{\bar{n},k+1} - \boldsymbol{X}^{\bar{n},k}) \right), \end{aligned} \tag{28}$$

where $s_\alpha^{\bar{n},k} = |\partial \boldsymbol{X}^{\bar{n},k} / \partial s|$ and $J_{\bar{n},k} = \partial \boldsymbol{F}_{mem} / \partial \boldsymbol{X}^{\bar{n},k}$. The last two terms in (28) is the linearization of the force $\bar{\boldsymbol{F}}_{mem}$ in (22). The update of $\boldsymbol{X}$ in iterations, from (23), is

$$\begin{aligned} &(k_w k_{ad} \mathbf{n}\mathbf{n}^T + I) \frac{\boldsymbol{X}^{n,k+1} - \boldsymbol{X}^n}{\Delta t} \\ &= S_{\bar{n},k}^* \boldsymbol{v}_c^{\bar{n},k+1} + k_w \left(\sigma^n + \frac{1}{s_\alpha^{\bar{n},k}} \left[\boldsymbol{F}_{mem}^{\bar{n},k} + J_{\bar{n},k} (\boldsymbol{X}^{\bar{n},k+1} - \boldsymbol{X}^{\bar{n},k}) \right] \cdot \mathbf{n} \right) \mathbf{n}. \end{aligned} \tag{29}$$

The normal vector in the iterations will be computed using $\boldsymbol{X}^{\bar{n},k}$. This fully implicit method and iteration scheme draw inspiration from the

second-order implicit IB scheme designed for a boundary mass problem with Navier–Stokes equations (Mori and Peskin, 2008).

We can first symbolically solve for the variable $\boldsymbol{v}_{\mathrm{c}}^{\bar{n},k+1}$ from (27) and (28) to get

$$\begin{aligned}\boldsymbol{v}_{\mathrm{c}}^{\bar{n},k+1} =& \frac{1}{\mu} L_h^{-1} P \Big\{ -\nabla \bar{p} - b\boldsymbol{v}_{\mathrm{c}}^{\bar{n},k} + \eta\theta_{\mathrm{n}}(\boldsymbol{v}_{\mathrm{n}}^{n} - \boldsymbol{v}_{\mathrm{c}}^{\bar{n},k}) + S_{\bar{n},k}(\sigma^n s_\alpha^{\bar{n},k}\mathbf{n} \\ & - k_{\mathrm{ad}} s_\alpha^{\bar{n},k}\mathbf{n}\mathbf{n}^{\mathrm{T}} \frac{\boldsymbol{X}^{n,k+1} - \boldsymbol{X}^{n}}{\Delta t} + \boldsymbol{F}_{\mathrm{mem}}^{\bar{n},k} + J_{\bar{n},k}(\boldsymbol{X}^{\bar{n},k+1} - \boldsymbol{X}^{\bar{n},k})) \Big\} .\end{aligned} \tag{30}$$

The operator $L^{-1}P$ involves solving the Stokes equation with appropriate projection and spreading terms (where the projection operator P ensures the continuity condition for all terms). Substituting (30) into (28), we observe the update for $\boldsymbol{X}^{\bar{n},k+1}$ in the form of a linear system

$$\mathcal{M}(\boldsymbol{X}^{n,k+1} - \boldsymbol{X}^{n,k}) = \Delta t \boldsymbol{z} - (k_{\mathrm{w}} k_{\mathrm{ad}} \mathbf{n}\mathbf{n}^{\mathrm{T}} + I)(\boldsymbol{X}^{n,k} - \boldsymbol{X}^{n}) \tag{31}$$

with

$$\mathcal{M} = (k_{\mathrm{w}} k_{\mathrm{ad}} \mathbf{n}\mathbf{n}^{\mathrm{T}} + I) - \frac{\Delta t}{2} \left[S_{\bar{n},k}^{*} \left(\frac{1}{\mu} L_h^{-1} P \right) S_{\bar{n},k} \left(J_{\bar{n},k} - \frac{2k_{\mathrm{ad}}}{\Delta t} s_\alpha^{\bar{n},k} \mathbf{n}\mathbf{n}^{\mathrm{T}} \right) + \frac{k_w}{s_\alpha^{\bar{n},k}} \mathbf{n}\mathbf{n}^{\mathrm{T}} J_{\bar{n},k} \right] \tag{32}$$

and

$$\begin{aligned}\boldsymbol{z} =& S_{\bar{n},k}^{*} \left[\frac{1}{\mu} L_h^{-1} P \Big\{ -G_h \bar{p} + \eta\theta_{\mathrm{n}}^{n}(\boldsymbol{v}_{\mathrm{n}}^{n} - \boldsymbol{v}_{\mathrm{c}}^{\bar{n},k}) + S_{\bar{n},k}(\sigma^n s_\alpha^{\bar{n},k}\mathbf{n} - k_{\mathrm{ad}} s_\alpha^{\bar{n},k}\mathbf{n}\mathbf{n}^{\mathrm{T}} \frac{\boldsymbol{X}^{n,k} - \boldsymbol{X}^{n}}{\Delta t} \\ & + \boldsymbol{F}_{\mathrm{mem}}^{\bar{n},k}) \Big\} + k_w \left(\sigma^n + \frac{1}{s_\alpha^{\bar{n},k}} \boldsymbol{F}_{\mathrm{mem}}^{\bar{n},k} \cdot \mathbf{n} \right) \mathbf{n} \right] .\end{aligned} \tag{33}$$

We employ an iterative method that minimizes the residual (Saad and Schultz, 1986) to solve the linear system (31). When we have $\|\Delta t \boldsymbol{z} - (k_{\mathrm{w}} k_{\mathrm{ad}} \mathbf{n}\mathbf{n}^{\mathrm{T}} + I)(\boldsymbol{X}^{n,k} - \boldsymbol{X}^{n})\| < \epsilon \|\boldsymbol{X}^{n}\|$ ($\epsilon = 10^{-7}$ in this work), we will set $\boldsymbol{X}^{n+1} = \boldsymbol{X}^{n,k+1}$, and $\boldsymbol{v}_{\mathrm{c}}^{n+1}$ will be obtained from the final update of (30).

3.2. Sub-step for actins

Both F-actin, θ_{n}, and G-actin, θ_{c}, concentrations are defined at cell centers, and their Eqs. (6) and (11) are characterized as advection-diffusion types within a dynamic domain. We employ a methodology used in our prior work (Yao and Mori, 2017) to handle the challenges posed by irregular cell centers and a mobile boundary. The inclusion of technical details in this section serves to provide a comprehensive understanding of our approach.

We first define the differencing operators applicable to any grid function w in the form

$$\begin{aligned} D_x^{\pm} w_{\alpha,\beta} &= \pm \frac{w_{\alpha\pm1,\beta} - w_{\alpha,\beta}}{h}, \quad D_y^{\pm} w_{\alpha,\beta} = \pm \frac{w_{\alpha,\beta\pm1} - w_{\alpha,\beta}}{h}, \\ \mathcal{L} w_{\alpha,\beta} &= D_x^{+} D_x^{-} w_{\alpha,\beta} + D_y^{+} D_y^{-} w_{\alpha,\beta} \\ &= \frac{w_{\alpha+1,\beta} + w_{\alpha,\beta+1} + w_{\alpha-1,\beta} + w_{\alpha,\beta-1} - 4w_{\alpha,\beta}}{h^2}, \end{aligned} \tag{34}$$

where $w_{\alpha,\beta}^{n}$ denotes the value of w at $(x, y) = (\alpha h, \beta h)$ at time $t = n\Delta t$.

3.3. Regular Cartesian grid centers

At any regular Cartesian cell center, we use a standard implicit Euler discretization of (6) in the form

$$\begin{aligned} & D_t^{-} \theta_{\mathrm{c}}{}_{i+\frac{1}{2},j+\frac{1}{2}}^{n+1} + D_x^{-} \left(u_{i+1,j+\frac{1}{2}}^{n+1} \mathcal{A}_x^{+} \theta_{\mathrm{c}}{}_{i+\frac{1}{2},j+\frac{1}{2}}^{n+1} \right) + D_y^{-} \left(v_{i+\frac{1}{2},j+1}^{n+1} \mathcal{A}_y^{+} \theta_{\mathrm{c}}{}_{i+\frac{1}{2},j+\frac{1}{2}}^{n+1} \right) \\ & = D_c \mathcal{L} \theta_{\mathrm{c}}{}_{i+\frac{1}{2},j+\frac{1}{2}}^{n+1} + \gamma \theta_{\mathrm{n}}^{n}, \end{aligned} \tag{35}$$

where, for any quantity w on the Cartesian grid, we have

$$\mathcal{A}_x^{+} w_{\alpha,\beta} = \frac{1}{2} \left(w_{\alpha+1,\beta} + w_{\alpha,\beta} \right) , \ \mathcal{A}_y^{+} w_{\alpha,\beta} = \frac{1}{2} \left(w_{\alpha,\beta+1} + w_{\alpha,\beta} \right) . \tag{36}$$

For the F-actin Eq. (11), the discretization at regular Cartesian cell centers are given by

$$\begin{aligned} & D_t^{-} \theta_{\mathrm{n}}{}_{i+\frac{1}{2},j+\frac{1}{2}}^{n+1} + \frac{1}{\eta + \eta_{\mathrm{st}}} D_x^{-} \left(u_{i+1,j+\frac{1}{2}}^{n+1} \mathcal{A}_x^{+} \theta_{\mathrm{n}}{}_{i+\frac{1}{2},j+\frac{1}{2}}^{n+1} \right) \\ & + \frac{1}{\eta + \eta_{\mathrm{st}}} D_y^{-} \left(v_{i+\frac{1}{2},j+1}^{n+1} \mathcal{A}_y^{+} \theta_{\mathrm{n}}{}_{i+\frac{1}{2},j+\frac{1}{2}}^{n+1} \right) \\ & = \frac{k_{\sigma_{\mathrm{n}}}}{\eta + \eta_{\mathrm{st}}} \mathcal{L} \theta_{\mathrm{n}}{}_{i+\frac{1}{2},j+\frac{1}{2}}^{n+1} - \gamma \theta_{\mathrm{n}}^{n+1}, \end{aligned} \tag{37}$$

3.4. Irregular Cartesian grid centers

At the irregular point A in Fig. 1(A), we employ a discretization method for θ_{c} and θ_{n} to extrapolate to the point p_1. For instance, the extrapolation for θ_{c} is (Macklin and Lowengrub, 2008)

$$\theta_{\mathrm{c}}{}_{p_1} = \frac{2(1-\rho)}{2+\rho} \theta_{\mathrm{c}}{}_{p_6} - \frac{3(1-\rho)}{1+\rho} \theta_{\mathrm{c}}{}_{p_5} + \frac{6}{(1+\rho)(2+\rho)} \theta_{\mathrm{c}}{}^{\mathrm{b}}, \tag{38}$$

where ρ is the ratio of distance from the grid crossing $(x_1^{\mathrm{b}}, y_1^{\mathrm{b}})$ to A and distance from p_1 to A (grid spacing in the y direction), $\theta_{\mathrm{c}}{}_{p_6}$ and $\theta_{\mathrm{c}}{}_{p_5}$ are the G-actin concentration at p_6 and p_5, respectively, and $\theta_{\mathrm{c}}{}^{\mathrm{b}}$ is the auxiliary G-actin concentration defined at the grid crossing $(x_1^{\mathrm{b}}, y_1^{\mathrm{b}})$. A similar procedure can be performed in the x direction to obtain an extrapolation formula at point p_3.

3.5. Treatment of freshly cleared grids

Consider the point F in Fig. 1(B). It is a freshly cleared point that was in Ω_{E} at time $t = n\Delta t$ but is in Ω_{I} at $t = (n+1)\Delta t$. When evaluating the time differencing terms, such as in (35) and (37), at this point, $\theta_{\mathrm{c}}{}_F^{n}$ and $\theta_{\mathrm{n}}{}_F^{n}$ must be available. Here, we employ a stable scheme for discretizing the time derivative (Yao and Mori, 2017). The following steps use $\theta_{\mathrm{c}}{}_F^{n}$ as an example, but the same procedure applies to $\theta_{\mathrm{n}}{}_F^{n}$ as well.

First, we identify the point $p_F = (x_F^*, y_F^*)$ on the curve Γ_n that is closest to the given point $F = (x_F, y_F)$. The G-actin concentration at this point p_F at time $t = n\Delta t$ (represented as $\theta_{\mathrm{c}}^{\mathrm{b}n}$) can be determined through interpolation of the G-actin concentration values at all grid crossings at the same time $t = n\Delta t$. If we approximate the partial time derivative at point F as

$$\frac{\theta_{\mathrm{c}}{}_F^{n+1} - \theta_{\mathrm{c}}^{\mathrm{b}n}}{\Delta t} , \tag{39}$$

it is not a pure temporal discretization because it contains an advective component due to the movement of the boundary. The velocity of this advection is given by

$$(\widetilde{u}_F, \widetilde{v}_F) = \left(\frac{x_F - x_F^*}{\Delta t}, \frac{y_F - y_F^*}{\Delta t} \right) . \tag{40}$$

Therefore, (39) must be corrected to remove the advective component resulting from the above velocity. The following is a modified discretization of the time derivative of concentration $\theta_{\mathrm{c}F}$ at point F:

$$\left. \frac{\partial \theta_{\mathrm{c}F}}{\partial t} \right|_{t=n\Delta t} \approx \frac{\theta_{\mathrm{c}}{}_F^{n+1} - \theta_{\mathrm{c}}^{\mathrm{b}n}}{\Delta t} - \widetilde{u}_F D_x^0 \theta_{\mathrm{c}}{}_F^{n+1} - \widetilde{v}_F D_y^0 \theta_{\mathrm{c}}{}_F^{n+1} , \tag{41}$$

where the operator $D_{x,y}^0$ is defined by

$$D_{x,y}^0 = \frac{1}{2} \left(D_{x,y}^{+} + D_{x,y}^{-} \right) . \tag{42}$$

At freshly cleared points, we substitute expression (41) for the $D_t^{-}\theta_{\mathrm{c}}$ term in (35). This modification is based on our earlier work (Yao and Mori, 2017), where further details can be found. The spatial differencing in these instances often involves ghost cell locations. In such scenarios, we employ the extrapolation formulas detailed in Section 3.4.

3.6. Enforcing boundary conditions at grid crossings

By introducing auxiliary variables $\theta_{\mathrm{c}}^{\mathrm{b}}$ and $\theta_{\mathrm{n}}^{\mathrm{b}}$, we enforce boundary conditions for both F-actin (12) and G-actin (7) at the grid crossings, illustrated by the point (x_1^b, y_1^b) in Fig. 1(A). Particular attention is given to the directional derivative. Further details can be found in our early work (Yao and Mori, 2017).

The unit normal direction $\mathbf{n}$ along Γ can be resolved into two components: along the grid line $\boldsymbol{v}_a$ (from point A to p_1) and off the grid line $\boldsymbol{v}_o$ (from boundary point (x_1^b, y_1^b) through grid point B and stopping on the grid line between C and p_7). Therefore, we express $\mathbf{n}$ as $\mathbf{n} = a_o\boldsymbol{v}_o + a_a\boldsymbol{v}_a$. Utilizing these two directions, the normal derivative $\nabla\theta_{\mathrm{c}}^{\mathrm{b}} \cdot \mathbf{n}$ (and $\nabla\theta_{\mathrm{n}}^{\mathrm{b}} \cdot \mathbf{n}$) can be decomposed as a linear combination of directional derivatives along the $\boldsymbol{v}_o$ and $\boldsymbol{v}_a$ directions in the forms

$$\nabla\theta_{\mathrm{c}}^{\mathrm{b}} \cdot \mathbf{n} = a_o \nabla\theta_{\mathrm{c}}^{\mathrm{b}} \cdot \boldsymbol{v}_o + a_a \nabla\theta_{\mathrm{c}}^{\mathrm{b}} \cdot \boldsymbol{v}_a = a_o \|\boldsymbol{v}_o\| \frac{\partial\theta_{\mathrm{c}}^{\mathrm{b}}}{\partial(\boldsymbol{v}_o/\|\boldsymbol{v}_o\|)} + a_a \|\boldsymbol{v}_a\| \frac{\partial\theta_{\mathrm{c}}^{\mathrm{b}}}{\partial(\boldsymbol{v}_a/\|\boldsymbol{v}_a\|)}. \tag{43}$$

When approximating partial derivatives along $\boldsymbol{v}_o$ and $\boldsymbol{v}_a$, we employ interior actin values. A first-order approximation is expressed as

$$\nabla\theta_{\mathrm{c}}^{\mathrm{b}} \cdot \mathbf{n} \approx a_o(\theta_{\mathrm{c}B} - \theta_{\mathrm{c}}^{\mathrm{b}}) + a_a(\theta_{\mathrm{c}p_5} - \theta_{\mathrm{c}}^{\mathrm{b}}), \tag{44}$$

where $\theta_{\mathrm{c}B}$ represents the G-actin concentration at point B, and $\theta_{\mathrm{c}}^{\mathrm{b}}$ is the auxiliary G-actin concentration at the grid crossing (x_1^b, y_1^b). The direction vectors are given by

$$\boldsymbol{v}_o = (x_B - x_1^b, y_B - y_1^b), \ \boldsymbol{v}_a = (x_{p_5} - x_1^b, y_{p_5} - y_1^b). \tag{45}$$

We employ higher-order approximations when additional cell centers are accessible. For instance, instead of solely relying on point B for the off-grid line direction, we may incorporate points B, C, and p_7 to enhance the accuracy of our approximation, in the form

$$\frac{\partial\theta_{\mathrm{c}}^{\mathrm{b}}}{\partial(\boldsymbol{v}_o/\|\boldsymbol{v}_o\|)} \approx -\frac{3}{2\|\boldsymbol{v}_o\|}\theta_{\mathrm{c}}^{\mathrm{b}} + \frac{2}{\|\boldsymbol{v}_o\|}\theta_{\mathrm{c}B} - \frac{1}{2\|\boldsymbol{v}_o\|}\left[(1-\rho)\theta_{\mathrm{c}C} + \rho\theta_{\mathrm{c}p_7}\right], \tag{46}$$

and if the grid crossing, point p_5 and p_6 are used, we have

$$\frac{\partial\theta_{\mathrm{c}}^{\mathrm{b}}}{\partial(\boldsymbol{v}_a/\|\boldsymbol{v}_a\|)} \approx -\frac{1+\rho}{(2+\rho)\Delta y}\theta_{\mathrm{c}p_6} + \frac{2+\rho}{(1+\rho)\Delta y}\theta_{\mathrm{c}p_5} - \frac{3+2\rho}{(1+\rho)(2+\rho)\Delta y}\theta_{\mathrm{c}}^{\mathrm{b}}. \tag{47}$$

The symbol ρ appearing in both (46) and (47) is identical to the one defined in (38).

3.7. Time splitting

Equipped with the foundations laid out in Sections 3.4, 3.5, and 3.6, we are poised to progress with the evolution of the actin components. Following our time-splitting approach, we initially update (7) and (35), utilizing the newly computed $\boldsymbol{X}^{n+1}$ and $\boldsymbol{v}_{\mathrm{c}}^{n+1}$ from the preceding substep dedicated to fluid–structure interaction. Subsequently, we proceed to update (12) and (37), leveraging the just-updated $\theta_{\mathrm{c}}^{n+1}$. Once $\theta_{\mathrm{n}}^{n+1}$ is determined, we circle back to reinitiate the first substep, advancing the fluid–structure interaction to sustain the ongoing time evolution.

4. Results and discussion

4.1. Parameters

The actin polymerization flux at the cell membrane is given by (5). In actin-driven cell migration, the overall impact of actin polymerization is predominantly localized at the leading edge of the cell (Craig et al., 2012). To depict this profile, we employ a smoothed step function in the form

$$j(s) = j_0\left(\tanh\left(\frac{s^6}{d_w}\right) + \tanh\left(\frac{(2\pi - s)^6}{d_w}\right) - 2\right), \quad s \in [0, 2\pi), \tag{48}$$

where j_0 and d_w are constants that control the strength and width of the flux, respectively. This profile as a function of material coordinate s is maintained at all times as cells migrate. A larger d_w leads to a wider distribution of the region of actin polymerization (two sample profiles of $j(s)$ on a circular cell of two different d_w values are provided in Fig. 4). In the model, we let $j_0 = 100$ nm/s and $d_w = 1$ by default. The parameter j_0 governs the actin velocity, allowing it to span a broad range as observed in experiments (Babich et al., 2012). We will vary d_w to quantify the impact of the distribution of actin flux. The θ_0 in (5) is 0.1 mM (Pollard et al., 2000).

In addition to actin polymerization, the rate of actin depolymerization, γ, is also an essential parameter that affects cell migration and morphology. We set the default value of γ to be 4×10^{-2} s^{-1}, which is considered an intermediate rate based on our knowledge of the one-dimensional model (Yao et al., 2023). At the same time, we will vary γ as an essential part of our studies. γ and d_w are the two key parameters that we will investigate in this work.

The rest of the parameters used in the model are specified as follows. The viscosity of cytosol and the extracellular fluid is taken from that of water, $\mu = 1 \times 10^{-3}$ Pa s. The membrane water permeability is $k_w = 1 \times 10^{-12}$ m/(Pa s) (Li et al., 2019). Considering that the cell membrane is highly flexible lipid molecules, which do not behave like a standard elastic material nor bear significant stress, we let the effective stress coefficient of the membrane be a small number, $k_m = 10^{-6}$ kg/m/s^2, while preserving the numerical stability of the immersed boundary fluid–structure interaction scheme. The initial concentrations for F-actin and G-actin are chosen at 0.1 mM for each, a typical concentration for actin molecules (Pollard et al., 2000; Yao et al., 2023).

The diffusion coefficient of G-actin is taken as $D_c = 10^{-11}$ m^2/s (Kiuchi et al., 2011; Yao and Li, 2022; Yao et al., 2023). The ratio of the coefficient of the F-actin network stress, k_{σ_n}, and the coefficient of the strength of focal adhesion, η_{st}, i.e., $k_{\sigma_n}/\eta_{\mathrm{st}}$, approximates the effective diffusion coefficient of F-actin. Since the F-actin network is less diffusive than the G-actin monomers in the cytosol, this ratio should be less than D_c. On the other hand, the ratio must not be too small to ensure the numerical stability of the system. Therefore, we let $k_{\sigma_n} = 10^{-3}$ kg m^2/s^2/mol and $\eta_{\mathrm{st}} = 2 \times 10^8$ kg/s/mol. The coefficient of interfacial stress between cytosol and the actin-network, η, is several orders of magnitude smaller than the coefficient of the strength of focal adhesion (Li and Sun, 2018; Li et al., 2019; Yao and Li, 2022; Yao et al., 2023). So, in this model, we let $\eta = 10^4$ kg/s/mol.

The resistant coefficient, k_{ad}, depends on the cell type and the properties of the substrate that cells reside on. Therefore, it becomes a free parameter for modeling purpose and controls the overall velocity of cell migration, which also depends on cell types. A reasonable range of cell velocity is on the order of 10 nm/s to 30 nm/s (Kiuchi et al., 2007; Gardel et al., 2008; Vitriol et al., 2015). Hence, in this model, we let $k_{\mathrm{ad}} = 10^3$ kg/m^2/s.

The computational parameters are listed as follows. Time step: $\Delta t = 0.005$ s. Spatial resolution: 256 grids along each of the x and y direction; 320 grids on the cell membrane (the material points). At the boundary of the computational domain, $\partial\Omega$, we use the conditions that have been used in our prior models (Li et al., 2019; Yao and Li, 2022): Periodic boundary conditions are enforced at $x = 0$ and $x = L$ to mimic an infinite domain length along the migration direction, whereas rigid-wall conditions are applied at $y = 0$ and $y = L$ to represent a finite domain width along the transverse direction. While the domain width choice impacts the hydraulic resistance on the cell (Maity et al., 2019; Li et al., 2019), it does not alter the conclusion of this study, which centers on actin-driven cell migration.

4.2. Model captures the cell migration and morphology

Our computational model initiates with a circular cell, having a diameter of 40 μm within the computational domain, a size consistent with a typical mammalian cell when attached to a substrate. The cell undergoes evolution and migration based on specified biophysical processes outlined in the model. Without loss of generality, we let the

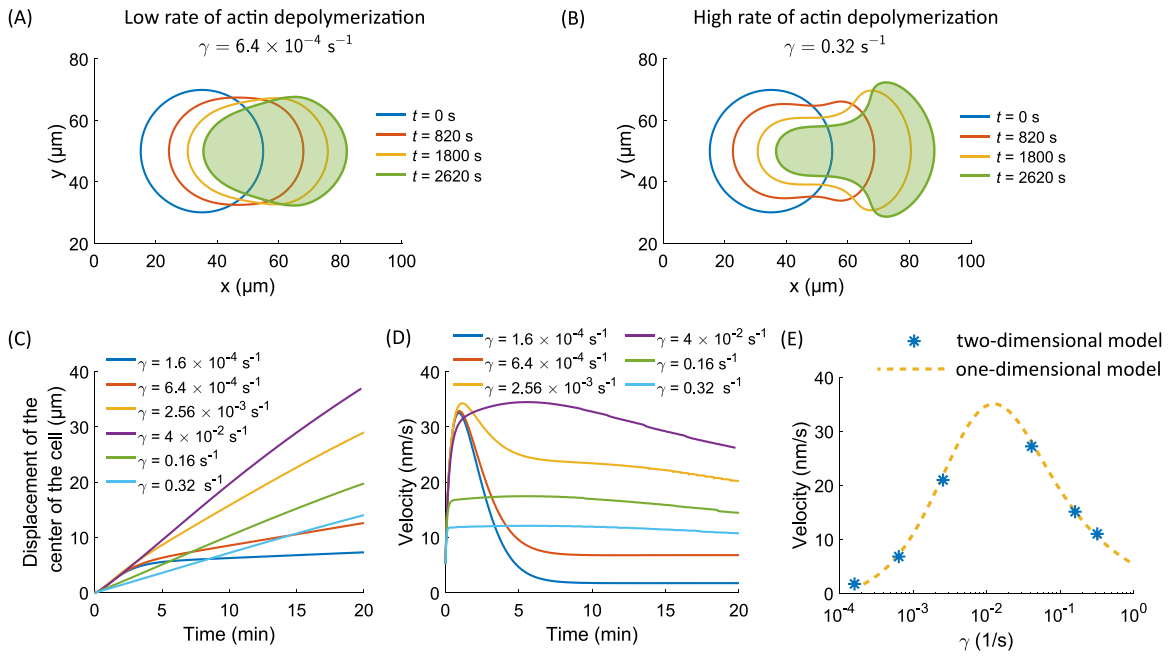

Fig. 2. Cell shape and velocity evolution for different rates of actin depolymerization, γ. (A) Cell shapes for a low rate of actin depolymerization. $\gamma = 6.4 \times 10^{-4}$ s^{-1}. (B) Cell shapes for a high rate of actin depolymerization. $\gamma = 0.32$ s^{-1}. The initial positions of the cells are at $x = 35$ μm and $y = 50$ μm. (C) The x−displacement of the center of cells as a function of time for different rates of actin depolymerization. (D) The velocity of the center of cells as a function of time for different rates of actin depolymerization. (E) Cell velocities as a function of the rate of actin depolymerization, γ. The velocities were extracted from the velocity curve at $t = 18$ min for all γ values in (D). Star: velocity data from this two-dimensional model. Dotted line: the shape of the biphasic velocity curve from our one-dimensional model in Yao et al. (2023) (Fig. 2C, $k_{\sigma_n} = 3 \times 10^4$ Pa/mM). The aspect ratio and position of the original curve were adjusted by $V_{2D}(\log \gamma) = c_1 V_{1D}(c_2 \log \gamma - c_3)$, where $c_1 = 0.97$, $c_2 = 1.27$, and $c_3 = 0.35$.

cell migrates along the x-direction from left to right. This is achieved by locating the actin flux (48) to the right-side of the cell. The initial conditions set the intracellular F-actin and G-actin concentrations to be spatially uniform, while the cytosol and F-actin velocities commence at zero. The implementation of G-actin in the model, coupled with implicit cytosol treatment, is able to achieve numerical stability across a broad range of parameters. In the subsequent sections, we will utilize representative model predictions to elucidate key biophysical mechanisms underpinning the influences of actin dynamics in cell dynamics.

A key characteristic of cell migration is the cell's spatial translocation, often accompanied by potential changes in morphology over time. A successful model should adeptly capture these details, facilitated by a clear visualization tool. Our model demonstrates robustness in modeling cell migration, showcasing the ability to predict diverse cell morphologies under different parameter settings. For instance, the shape of the cell evolves distinctively for varying rates of actin depolymerization, γ, while keeping other parameters constant (Fig. 2A, B). This model prediction underscores the significant influence of intracellular actin dynamics on cell morphology.

The cell's displacement over time can be tracked by utilizing its geometrical center. As anticipated, cells with different rates of actin depolymerization exhibit distinct time trajectories (Fig. 2C), allowing the calculation of cell velocity at each time point. The cell velocity displays an initial peak before reaching a plateau (Fig. 2D). Notably, the cell velocity varies with increasing rates of actin depolymerization. For low values of γ, the initial peak is narrow and short, while for higher values of γ, the duration and width of the initial peak proportionally increase. This initial peak is attributed to the initial cell deformation deviating from a circle, in addition to the migration velocity, given that the velocity is calculated from the geometrical center of the cell. As the impact from the initial cell deformation diminishes over time, the calculated velocity of the cell from its geometrical center aligns with the overall translational cell migration velocity.

In our previous one-dimensional model, we identified a biphasic pattern in cell velocity as a function of the rate of actin depolymerization: excessively high or low rates were suboptimal for cell migration (Yao et al., 2023). This is because low rates of actin depolymerization correspond to low rates of actin retrograde flow (Eq. (4)), slowing down cell migration, whereas high rates of actin depolymerization lead to reduced F-actin concentration (Eq. (3)), providing less structure to support driving forces from focal adhesion (Eq. (8)) (Yao et al., 2023). Remarkably, our two-dimensional model also predicts a biphasic trend in cell velocity as a function of γ (Fig. 2E). Moreover, when we superimpose the one-dimensional biphasic velocity curve (Yao et al. (2023), Fig. 2C, with an adjustment of the aspect ratio while keeping the curve's shape intact) onto the predicted cell velocity from this two-dimensional model, we observe a remarkable match. The consistency between the one-dimensional and two-dimensional model predictions not only underscores the successful implementation of the two-dimensional model and numerical algorithm but also confirms the robust biophysical implication of the biphasic dependence of cell velocity on the rate of actin depolymerization. Here, we emphasize that the match does not pertain to the absolute velocities between the two models, but rather to the scaling of cell velocities relative to the rate of actin depolymerization. The absolute velocities are contingent upon the parameters within each model. Nevertheless, we can adjust the aspect ratios of these curves to attain a satisfactory alignment between them.

4.3. Low rates of actin depolymerization leads to negligible transverse variations

Our one-dimensional model revealed that the spatial distribution of F-actin depends on the rate of actin depolymerization, γ (Yao et al., 2023). Specifically, high rate of actin depolymerization leads to highly polarized F-actin to the cell front. The two-dimensional model shows a consistent trend of actin distribution on the rate of actin depolymerization. For a small γ, the F-actin concentration decreases slowly from the leading edge to the trailing edge, with an almost consistent slope

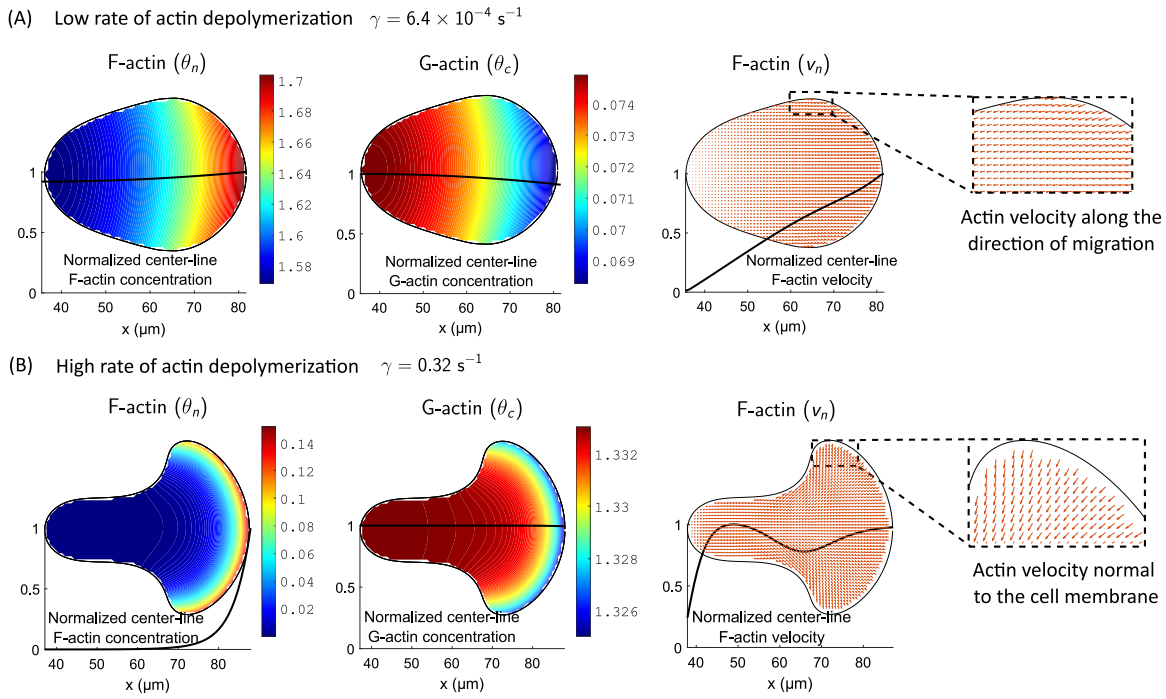

Fig. 3. Actin profiles for different rates of actin depolymerization, γ. The two snapshots are taken at $t = 2620$ s, corresponding to the last trajectories in Fig. 2A, B. (A) $\gamma = 6.4\times10^{-4}$ s^{-1}, representing a low rate of actin depolymerization. (B) $\gamma = 0.32$ s^{-1}, representing a high rate of actin depolymerization. θ_n: concentration of F-actin. θ_c: concentration of G-actin. v_n: velocity of F-actin. The unit of the color bar is 0.1 mM. The line plots display normalized values extracted from the center line of each two-dimensional profile.

throughout the cell (Fig. 3A, θ_n). On the other hand, for a large γ, most of the F-actin concentrated at the cell leading edge and decreases sharply away from the edge (Fig. 3B, θ_n). This arises because, according to (11), the distribution of F-actin approximates an exponential form (when cytosol velocity is minimal, which is the case in this work), characterized by a length scale $L_F \sim (D_n/\gamma)^{1/2}$, where D_n represents the effective diffusion coefficient of the F-actin network. L_F indicates the distance over which F-actin can redistribute (i.e., D_n) when it undergoes consumption (i.e., γ). As γ increases, L_F decreases, thereby enhancing the exponential decay of F-actin away from the leading edge.

The spatial gradient of G-actin concentration shows the opposite sign, such that the concentrations at the trailing edge is higher than that at the leading edge (Fig. 3A, B, θ_c). However, except for every small values of γ as illustrated in Fig. 3(A), the spatial gradient of G-actin is much smaller compared to that of F-actin. The larger the γ, the smaller the gradient of G-actin, leading to an almost constant G-actin concentration in the cell (Fig. 3B). The relation on G-actin gradient and γ can also be analyzed by scaling laws. With negligible cytosol velocity, Eq. (6) suggests that the length scale of G-actin variation is $L_G \sim (D_c/\gamma)^{1/2}(\theta_c/\theta_n)$. The ratio θ_c/θ_n is on the order of $\gamma L/j_0$ (Yao et al., 2023), where L is the length scale of the cell. Therefore, we have $L_G \sim (D_c\gamma)^{1/2}(L/j_0)$, which increases as γ increases. All these results depicting the distribution of F-actin and G-actin with respect to γ align well with the one-dimensional model prediction (Yao et al., 2023).

The limitation of a one-dimensional model is that we have to consider scenarios where cells are confined to a one-dimensional space or when to assume that intracellular quantities predominantly vary along the longitudinal direction (parallel to cell migration), with minimal transverse variations (Li et al., 2019; Yao et al., 2023). While this one-dimensional model has proven successful in modeling confined cell migration (Zhang et al., 2022; Bera et al., 2022), the extent and conditions under which it is applicable to two-dimensional, open-space cell migration scenarios remain uncertain. If a two-dimensional cell migration mimics a one-dimensional case, the spatial variation of intracellular fields, such as actin concentration and velocity, should primarily occur along one direction while remaining relatively constant in the orthogonal direction. Our two-dimensional model predicts that, for low rates of actin depolymerization, the cell behaves similarly to a one-dimensional object, with F-actin concentration (θ_n), G-actin concentration (θ_c), and F-actin velocity (v_n) predominantly varying along the direction of migration (x) but maintaining nearly constant profiles along the transverse direction (y) (Fig. 3A). The two-dimensional model provide insights into non-confined *in vivo* cell migration: For cells migrating in scenarios with low actin depolymerization rates, the one-dimensional approximation might be a reasonable first-order approach.

4.4. High rates of actin depolymerization spreads the cell leading edge

As the actin depolymerization rate increases, we have seen that the cell evolves into distinct morphology compared to the low rate of actin polymerization (Fig. 2A,B). In this case, the spatial profiles of the F-actin concentration (θ_n), G-actin concentration (θ_c), and F-actin velocity (v_n) exhibit noticeable spatial gradients along both the migration direction (x) and the transverse direction (y) (Fig. 3B). This suggests that at higher depolymerization rates, two-dimensional effects cannot be ignored, and models accounting for full spatial complexity are necessary to accurately capture the dynamics of cell migration.

The cell exhibits a distinctive fan-like spreading leading edge and a narrow rod-like trailing edge, reminiscent of migrating fish keratocytes (Keren et al., 2008, 2009). This unique morphology is intimately linked to the F-actin velocity profile at the leading edge. Closer examination reveals that at high depolymerization rates, actin retrograde flow is always perpendicular to the membrane (Fig. 3B, θ_n). This perpendicular flow profile, driven by interactions with focal adhesion reactive forces (Li and Sun, 2018; Gardel et al., 2008), acts as the key driver of the spreading morphology. This type of spreading morphology is often seen in cells immersed in high-viscosity media (Gonzalez-Molina et al., 2018; Maity et al., 2022; Bera et al., 2022). However, at low rates of actin depolymerization, this distinctive feature disappears, with the flow reverting to a direction parallel to migration (Fig. 3A,

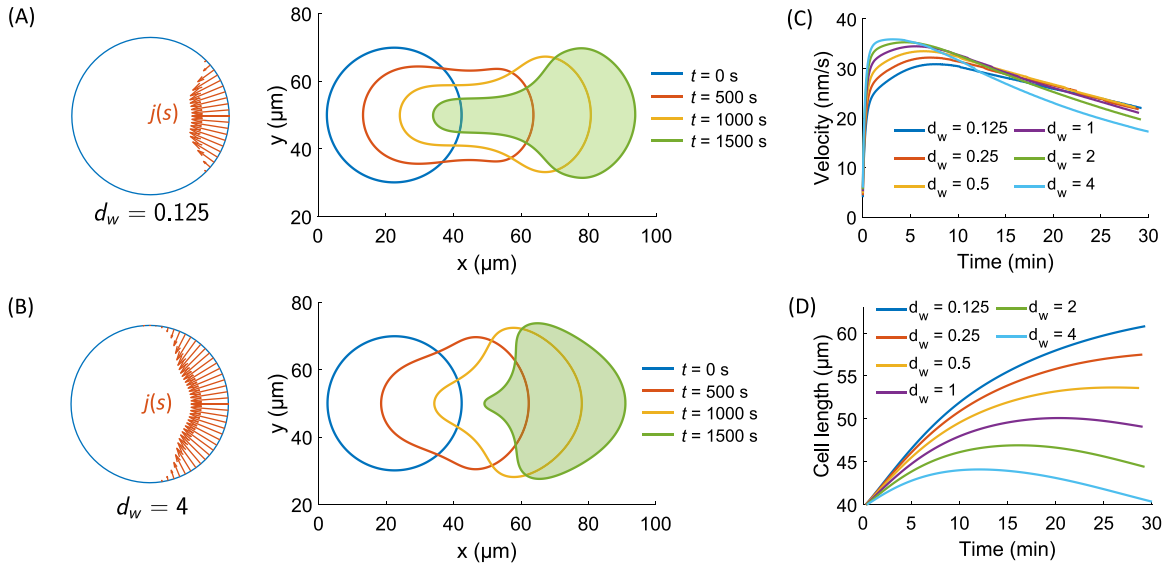

Fig. 4. Cell shape and velocity evolution for different widths of actin polymerization, d_w. In this set of simulations, $\gamma = 4 \times 10^{-2}$ s^{-1}, a moderate rate. (A) Cell shapes for a narrow distribution of actin polymerization. $d_w = 0.125$. (B) Cell shapes for a wide distribution of actin polymerization. $d_w = 4$. The initial positions of the cells are at $x = 22$ μm and $y = 50$ μm. The distribution of actin polymerization, $j(s)$, is calculated from Eq. (48) with the corresponding d_w values. (C) The velocity of the center of cells as a function of time for different widths of actin polymerization. (D) The length of cells as a function of time for different widths of actin polymerization. The cell length is calculated from the distance between the cell front (the right-most x-position) and the cell back (the left-most x-position).

θ_n). This finding suggests that actin retrograde flow directionality may be crucial for shaping cell migration morphology.

The direction of actin retrograde flow not only shapes cell morphology but also profoundly impacts cell velocity. When actin flow is unidirectional, the entire driving force points forward, preventing momentum from scattering in different directions. This allows cells to maintain a steady-state forward velocity in low depolymerization rates where cell velocities reaches a plateau after the initial transient period (Fig. 2D). However, when the flow becomes perpendicular to the membrane, momentum in the transverse direction (perpendicular to migration) also arises, reducing the energy available for longitudinal movement. This explains why in high depolymerization rates, cell velocity gradually decreases over time (Fig. 2D). Thus, understanding the interplay between actin flow direction and depolymerization rate provides key insights into the diverse migratory behaviors observed in different cellular contexts.

As anticipated, the transition from one-dimensional to two-dimen sional spatial variation lacks a definitive boundary. Building on our analysis of actin distribution using a one-dimensional model (Yao et al., 2023), the shift to a two-dimensional pattern becomes increasingly prominent as actin depolymerization rates begin to decrease cell velocity (the second phase of the biphasic curve).

4.5. Narrow distribution of actin polymerization elongates cells

The intricate interplay of actin polymerization and depolymerization shapes cell dynamics. We previously investigated the impact of depolymerization rates on cell migration. Next, we leverage our model to quantify how the distribution of actin polymerization influences these dynamics.

Our model predicts that a narrow distribution of actin polymerization, such as when $d_w = 0.125$, functions akin to a focused thrust. This actin flux drives the cell predominantly in a single direction, leading to elongation along the migration axis and resulting in a shape reminiscent of a measuring spoon (Fig. 4A). In contrast, a wide distribution, exemplified by $d_w = 4$, encourages a more extensive leading edge that spreads moderately with minimal elongation. This broader polymerization footprint shapes the cell into a form resembling a scallop shell (Fig. 4B). This aligns with our intuition: the extent of leading edge spreading directly correlates with the width of the actin polymerization zone. Nevertheless, the spreading morphology observed in this case differs from that under high rates of actin depolymerization (Fig. 2B), where the actin concentration gradient is distinctly pronounced close to the cell boundary.

The cell velocity is also influenced by the width of the distribution of actin polymerization (Eq. (48), Fig. 4C). Under narrow distributions of actin polymerization, the velocities do not experience a significant decrease beyond the initial peak. In contrast, for wide distributions of actin polymerization, the cell velocity steadily drops after the initial peak. This behavior is notable when cells undergo spreading at the leading edge, as discussed in Section 4.4. The distinct velocity patterns observed under different actin polymerization widths emphasize the impact of polymerization distribution on cell motility.

Moreover, the model establishes a connection between the width of the actin polymerization zone and cell morphology. Narrow distributions of actin polymerization drive cell elongation (Fig. 4D), where the narrower the distribution, the longer the cell stretches. This discovery directly correlates with observed filopodia in living cells – slender, finger-like protrusions rich in actin bundles formed through continuous polymerization at their tips (Faix and Rottner, 2006; Medalia et al., 2007; Le Clainche and Carlier, 2008; Mattila and Lappalainen, 2008). The strength of our model lies in its ability to translate microscopic actin dynamics into macroscopic cellular behavior. Despite operating at the whole-cell level, it effectively represents local membrane protrusions like filopodia, which illustrates that localized actin polymerization leads to cell tip extension. In actual cells, actin dynamics rarely exhibit uniformity or a steady state. The dynamic adjustment of the actin profile *in vivo* contributes to shaping the protrusion morphology of filopodia, often rendering it more pointed than our model predicts. Remarkably, our model's predictions closely mirror the dynamic and

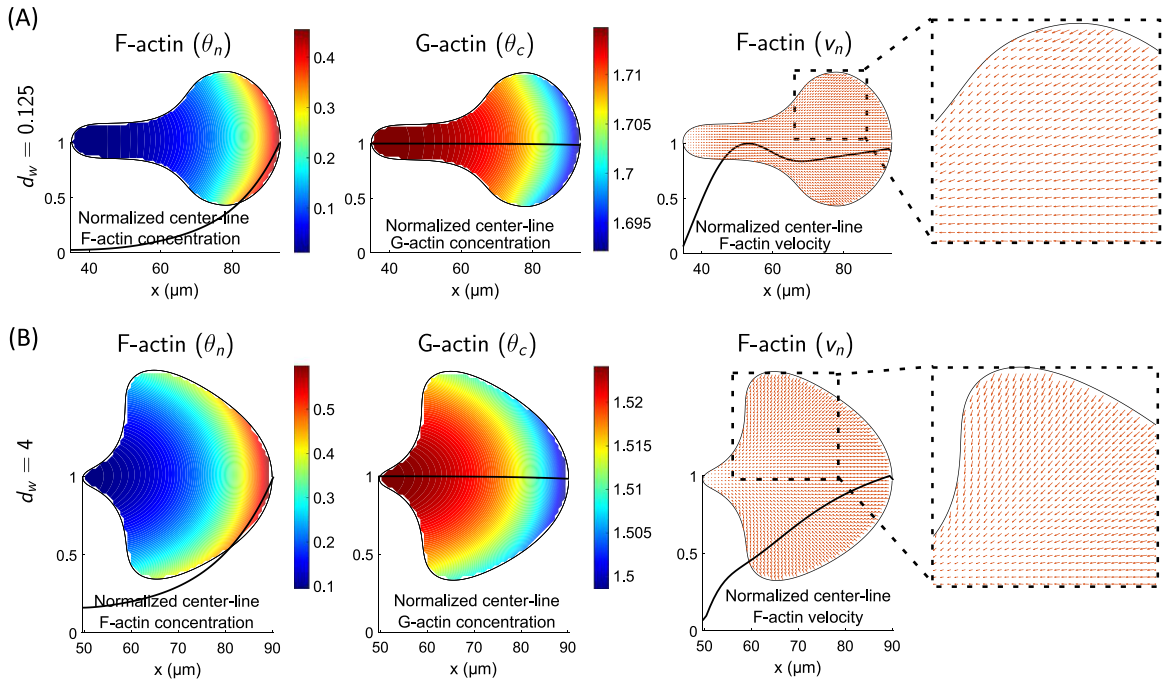

Fig. 5. Actin profiles for different widths of actin polymerization, d_w, extracted from the simulations presented in Fig. 4. The two snapshots are taken at $t = 1500$ s, corresponding to the last trajectories in Fig. 4A,B (A) $d_w = 0.125$, representing a narrow distribution of actin polymerization. (B) $d_w = 4$, representing a wide distribution of actin polymerization. θ_n: concentration of F-actin. θ_c: concentration of G-actin. v_n: velocity of F-actin. The unit of the color bar is 0.1 mM. The line plots display normalized values extracted from the center line of each two-dimensional profile.

irregular morphology observed in mammalian cells, underscoring its potential to capture the intricate interplay of forces shaping cellular form.

4.6. Wide distribution of actin polymerization extends the effective region of intracellular F-actin

While the rate of actin depolymerization, γ, demonstrates a powerful influence on intracellular F-actin and G-actin distribution, we hypothesize that the boundary condition of actin polymerization also plays a significant role. Our model predicts that for narrow actin polymerization profiles, F-actin concentration undergoes a dramatic shift, forming a pronounced gradient in the head region that transitions to an almost plateau-like state in the remaining cell body (Fig. 5A, θ_n). Most of the F-actin is distributed towards the frontal boundary of the cell, making the effective region of F-actin limited. The concentration of G-actin (θ_c) shows the same trend in terms of gradient but with an opposite sign and negligible magnitude. Interestingly, actin velocity presents a contrasting picture. The magnitude of the velocity remains almost remains across the cell, except for a gentle fade at the rear tip where flow ceases (Fig. 5A, v_n). This uniform magnitude stands in stark contrast to the steep F-actin gradient, highlighting the complex interplay between concentration and flow dynamics. Away from the centerline, the velocity gradually develops a component perpendicular to the direction of migration. This component helps to shape the head region of the cell. This predicted persistence of F-actin velocity within the elongated cell resonates with experimental observations of strong actin retrograde flow in filopodia (Aratyn et al., 2007; Bornschlögl, 2013). Our model thus bridges the gap between molecular-level dynamics and observable cellular behavior, offering a deeper insight of cell migration and its diverse morphologies.

In contrast, wide distributions of actin polymerization show a vastly different picture of intracellular dynamics. As the leading edge broadens, the head region encompasses a significantly larger portion of the cell (Fig. 5B). This expansion translates into a large effective region of F-actin distribution, stretching the non-zero concentration regime across the entire cell body (Fig. 5B, θ_n). This smooth gradient coincides with a nearly uniform actin flow, as predicted by our model (Fig. 5B, θ_n). The well-developed, distributed flow stands very differently from the localized actin flow observed under high depolymerization rates (Fig. 3B, v_n), even though both cases have spreading cell leading edge. Our model demonstrates that actin dynamics emerge from a multifactorial interplay, not simply a one-perspective interpretation based on leading edge morphology.

Further examination into the differences between narrow and wide actin polymerization profiles, under identical depolymerization rates, reveals additional observations. First, cells with narrow profiles behave like one-dimensional systems. Their key variables, including F-actin and G-actin concentrations and actin flow, primarily vary along the migration axis, showing minimal differences across the cell width (Fig. 5A). Conversely, cells with wide profiles exhibit a true two-dimensional character. Here, all spatial variables display non-negligible transverse gradients, hinting at a more complex, multi-directional interplay of forces within the cell (Fig. 5B). Second, cells with wider actin polymerization profiles maintain higher average F-actin concentrations compared to their narrower counterparts (Fig. 5A, B, θ_n). This suggests that, beyond the influence of depolymerization rate, the distribution of actin polymerization impacts the total F-actin content within the cell. This finding has important implications, potentially indicating that a wider distribution helps maintain a more balanced intracellular actin dynamic.

5. Discussion and conclusions

In this study, we have developed a two-dimensional immersed boundary model to investigate cell migration influenced by actin polymerization and depolymerization. The crucial addition of a G-actin phase, absent in our previous models, enhances the depth of our analysis.

Our two-dimensional model effectively elucidates the impact of actin dynamics on shaping cell morphology and motility. Under conditions of low rates of actin depolymerization or narrow distributions

of actin polymerization, cells exhibit characteristics resembling a one-dimensional system, with spatial variables primarily varying along the direction of cell migration. Conversely, under high rates of actin depolymerization or wide distributions of actin polymerization, cells display two-dimensional features, including spreading in the transverse direction and transverse variation of actin concentration and velocities. Therefore, the two-dimensional cell migration model excels in portraying morphology and spatial variables.

While the one-dimensional model falls short in capturing cell morphology, especially under high rates of actin depolymerization, the consistency of actin dynamics along the cell's center line and cell velocity remains notable between our one-dimensional and two-dimensional models. In both models, high rates of actin depolymerization reduce the region of actin retrograde flow, decrease the total content of F-actin, and increase the total content of G-actin (Yao et al., 2023). Moreover, cell velocities are predicted to be biphasic as a function of the rate of actin depolymerization; the remarkable agreement of the biphasic curve (upon re-scaling) between the one-dimensional and two-dimensional models demonstrates the accuracy of the two-dimensional computational scheme. These compelling findings suggest that the intrinsic scales of cell velocity and actin distribution as functions of the rate of actin depolymerization are well-preserved in the two models.

The two-dimensional model provides unique insights beyond morphology, extending the understanding beyond what a one-dimensional model can offer. Specifically, the model establishes a connection between the microscopic aspects, such as the direction and amplitude of actin velocity (referred to as the actin retrograde flow), and macroscopic observables, such as cell morphology. Actin velocity aligned with the direction of cell migration tends to elongate the cell in that direction, facilitating migration. Conversely, velocity normal to the cell membrane tends to spread the cell at corresponding membrane locations. In many instances, actin velocity comprises both components along the direction of migration and normal to the cell membrane, representing simultaneous cell migration and spreading. Such phenomena are frequently observed in two-dimensional mammalian cell migration on a substrate.

To contextualize our discussion, we turn to experimental insights from the literature illustrating the influence of actin dynamics on cell morphology. Actin behavior is regulated by various physical and biochemical factors, including extracellular viscosity. High extracellular viscosity has been observed to modulate cell morphology, shifting cells from a blebbing-based phenotype to a protrusion-based phenotype (Gonzalez-Molina et al., 2018; Maity et al., 2022; Bera et al., 2022). For instance, in Extended Data Fig. 8(d) of Bera et al. (2022), cells were observed to initiate spreading when exposed to high-viscosity media, a process facilitated by actin network branching. This finding highlights that cell spreading entails both longitudinal and transverse actin dynamics, as evidenced by branching occurring in all directions within the two-dimensional space. This experimental observation aligns with our model's prediction that cell spreading corresponds to actin flow in multiple directions. This preliminary comparison between our model and experimental results lays the foundation for future comprehensive investigations.

In our study, we employed the immersed boundary method as a computational tool to investigate cell morphology and motility. There are other versatile moving boundary methods capable of achieving similar goals, such as the phase-field method (Shao et al., 2012) and the level-set method (Wolgemuth and Zajac, 2010). All three methods have been employed to study cell migration and significant cell deformations, such as those occurring during cytokinesis (Rejniak, 2007; Anderson et al., 2009; Li et al., 2017; Moure and Gomez, 2021). Each method possesses its unique strengths. For instance, both the phase-field and the level-set methods use a scalar variable to trace the cell boundary without explicitly model the fluid–structure interaction. This type of method brings computational efficiency. The immersed boundary method, on the other hand, relies on explicit modeling of the mechanics of the membrane and its mechanical interaction with the surrounding fluid. This scheme brings complicity of the numerical algorithm, but on the other hand enables detailed treatment of membrane mechanics. Although the membrane mechanics is not the focus of this work, we anticipate future development that elaborates on the membrane mechanics, thermal fluctuation, and membrane-actin interaction.

The two-dimensional model, capable of calculating the cell morphology, comes with high computational costs. For instance, given the current domain and grid sizes, a single simulation, such as the one depicted in Fig. 4(A), requires several days on a cluster. Increasing the domain size, reducing the grid size, or extending the simulation time would further escalate these computational demands. In this study, we opt to simulate cell migration over a thirty-minute period for two specific reasons: first, this duration allows us to observe the transformation of cell morphology from an initial circular form to a shape dictated by model parameters; second, this timeframe remains computationally manageable. Within this half-hour window, cell dynamics achieve a steady state for certain parameter sets, while for others, they remain transient.

The computational cost of a two-dimensional model can seem formidable, necessitating careful consideration of when it should be utilized. A two-dimensional model becomes indispensable when cells exhibit significant spatial variations in multiple directions or when changes in morphology are critical. Experimental observations on traditional two-dimensional dishes, such as those showing migrating cells undergoing simultaneous changes in direction and morphology (Wei et al., 2009), accompanied by actin repolarization in a two-dimensional space, exemplify this need. Additionally, cell spreading in viscous media (Maity et al., 2022; Bera et al., 2022) underscores situations where a two-dimensional model is beneficial. However, merely having a two-dimensional shape without significant multi-dimensional spatial variations in actin (as illustrated in Fig. 2A) does not justify using a two-dimensional model. Conversely, *in vivo* scenarios frequently confine cells tightly during migration, leading to elongated morphologies (Wolf et al., 2009; Petrie et al., 2014; Paul et al., 2017). In such cases, a one-dimensional model proves more suitable.

A neat alternative approach to investigating cell morphology, without relying on a two-dimensional framework, is to model cell dynamics along the membrane (Lomakin et al., 2015; Copos and Mogilner, 2020). This method enables the study of interactions among F-actin structures and G-actin along the cell periphery, thereby drawing implications for cell polarization. In addition to their application in confined cell migration or cell mechanics along membranes, one-dimensional models have also been utilized in other scenarios. For instance, when two-dimensional cells display circular symmetry, one-dimensional models can be developed along the radial direction to describe the conservation laws governing the flows of F-actin and G-actin (Appalabhotla et al., 2023). These models are valuable for studying actin protrusions along the cell membrane.

This study provides a robust foundation for investigating cell migration dynamics and their implications for various cellular processes, offering promising directions for future research. First, the model can be refined to enhance biophysical significance by incorporating additional factors such as myosin to better represent actin dynamics. Accounting for cell-substrate interactions and adapting the model to complex geometries can provide insights into cell migration in intricate biological contexts. Second, efforts can focus on bridging scales and linking the model to experiments by integrating live-cell imaging data and upscaling to multicellular systems. The model may also serve as a computational tool for drug discovery, screening potential drugs targeting actin dynamics and influencing cell migration. Delving into these

avenues positions the two-dimensional cell migration model as a powerful tool for understanding and manipulating cellular behavior across various fields, from fundamental biology to biophysical applications.

CRediT authorship contribution statement

Lingxing Yao: Writing – review & editing, Writing – original draft, Methodology, Investigation, Formal analysis, Data curation, Conceptualization. **Yizeng Li:** Writing – review & editing, Writing – original draft, Visualization, Supervision, Project administration, Methodology, Investigation, Funding acquisition, Formal analysis, Data curation, Conceptualization.

Declaration of competing interest

The authors declare that they have no known competing financial interests or personal relationships that could have appeared to influence the work reported in this paper.

Acknowledgments

Yizeng Li is supported by National Science Foundation (NSF) 2303648. The opinions, findings, and conclusions, or recommendations expressed are those of the authors and do not necessarily reflect the views of any of the funding agencies.

References

Alert, R., Trepat, X., 2020. Physical models of collective cell migration. Annu. Rev. Condens. Matter Phys. 11, 77–101.
Anderson, A.R.A., Rejniak, K.A., Gerlee, P., Quaranta, V., 2009. Microenvironment driven invasion: a multiscale multimodel investigation. J. Math. Biol. 58, 579–624.
Appalabhotla, R., Butler, M.T., Bear, J.E., Haugh, J.M., 2023. G-actin diffusion is insufficient to achieve F-actin assembly in fast-treadmilling protrusions. Biophys. J. 122 (18), 3816–3829.
Aratyn, Y.S., Schaus, T.E., Taylor, E.W., Borisy, G.G., 2007. Intrinsic dynamic behavior of fascin in filopodia. Mol. Biol. Cell. 18 (10), 3928–3940.
Babich, A., Li, S., O'Connor, R.S., Milone, M.C., Freedman, B.D., Burkhardt, J.K., 2012. F-actin polymerization and retrograde flow drive sustained plcγ1 signaling during t cell activation. J. Cell. Biol. 197 (6), 775–787.
Baeyens, A.A.L., Schwab, S.R., 2020. Finding a way out: S1P signaling and immune cell migration. Annu. Rev. Immunol. 38, 759–784.
Bera, K., Kiepas, A., Godet, I., Li, Y., Mehta, P., Ifemembi, B., Paul, C.D., Sen, A., Serra, S.A., Stoletov, K., Tao, J., Shatkin, G., Lee, S.J., Zhang, Y., Boen, A., Mistriotis, P., Gilkes, D.M., Lewis, J.D., Fan, C.-M., Feinberg, A.P., Valverde, M.A., Sun, S.X., Konstantopoulos, K., 2022. Extracellular fluid viscosity enhances cell migration and cancer dissemination. Nature 611 (7935), 365–373.
Blackley, D.G., Cooper, J.H., Pokorska, P., Ratheesh, A., 2021. Mechanics of developmental migration. In: Seminars in Cell & Developmental Biology.
Bornschlögl, T., 2013. How filopodia pull: what we know about the mechanics and dynamics of filopodia. Cytoskeleton 70 (10), 590–603.
Copos, C., Mogilner, A., 2020. A hybrid stochastic-deterministic mechanochemical model of cell polarization. Mol. Biol. Cell 31 (15), 1637–1649.
Craig, E.M., Van Goor, D., Forscher, P., Mogilner, A., 2012. Membrane tension, myosin force, and actin turnover maintain actin treadmill in the nerve growth cone. Biophys. J. 102 (7), 1503–1513.
Dembo, M., Harlow, F., 1986. Cell motion, contractile networks, and the physics of interpenetrating reactive flow. Biophys. J. 50 (1), 109–121.
Faix, J., Rottner, K., 2006. The making of filopodia. Curr. Opin. Cell Biol. 18 (1), 18–25.
Gardel, M.L., Sabass, B., Ji, L., Danuser, G., Schwarz, U.S., Waterman, C.M., 2008. Traction stress in focal adhesions correlates biphasically with actin retrograde flow speed. J. Cell. Biol. 183 (6), 999–1005.
Gonzalez-Molina, J., Zhang, X., Borghesan, M., da Silva, J.M., Awan, M., Fuller, B., Gavara, N., Selden, C., 2018. Extracellular fluid viscosity enhances liver cancer cell mechanosensing and migration. Biomaterials 177, 113–124.
Inagaki, N., Katsuno, H., 2017. Actin waves: Origin of cell polarization and migration?. Trends Cell Biol. 27 (7), 515–526.
Jorgensen, S.N., Sanders, J.R., 2016. Mathematical models of wound healing and closure: a comprehensive review. Med. Biol. Eng. Comput. 54 (9), 1297–1316.
Keren, K., Pincus, Z., Allen, G.M., Barnhart, E.L., Marriott, G., Mogilner, A., Theriot, J.A., 2008. Mechanism of shape determination in motile cells. Nature 453 (7194), 475–480.
Keren, K., Yam, P.T., Kinkhabwala, A., Mogilner, A., Theriot, J.A., 2009. Intracellular fluid flow in rapidly moving cells. Nat. Cell. Biol. 11 (10), 1219–1224.
Kim, Y., Peskin, C.S., 2006. 2-D parachute simulation by the immersed boundary method. SIAM J. Sci. Comput. 28, 2294–2312.
Kim, D.-H., Provenzano, P.P., Smith, C.L., Levchenko, A., 2012. Matrix nanotopography as a regulator of cell function. J. Cell. Biol. 197 (3), 351–360.
Kiuchi, T., Nagai, T., Ohashi, K., Mizuno, K., 2011. Measurements of spatiotemporal changes in g-actin concentration reveal its effect on stimulus-induced actin assembly and lamellipodium extension. J. Cell. Biol. 193 (2), 365–380.
Kiuchi, T., Ohashi, K., Kurita, S., Mizuno, K., 2007. Cofilin promotes stimulus-induced lamellipodium formation by generating an abundant supply of actin monomers. J. Cell. Biol. 177 (3), 465–476.
Kozlov, M.M., Mogilner, A., 2007. Model of polarization and bistability of cell fragments. Biophys. J. 93 (11), 3811–3819.
Le Clainche, C., Carlier, M., 2008. Regulation of actin assembly associated with protrusion and adhesion in cell migration. Physiol. Rev. 88 (2), 489–513.
Li, Y., He, L., Gonzalez, N.A.P., Graham, J., Wolgemuth, C., Wirtz, D., Sun, S.X., 2017. Going with the flow: Water flux and cell shape during cytokinesis. Biophys. J. 113, 2487–2495.
Li, Y., Sun, S.X., 2018. Transition from actin-driven to water-driven cell migration depends on external hydraulic resistance. Biophys. J. 114, 2965–2973.
Li, Y., Sun, S.X., 2024. Cell migration dynamics explained by the coupling of mechanics with electrochemistry and ph regulation. Phys. Rev. Res. 6, 023158.
Li, Y., Yao, L., Mori, Y., Sun, S.X., 2019. On the energy efficiency of cell migration in diverse physical environments. Proc. Natl. Acad. Sci. USA 116 (48), 23894–23900.
Lomakin, A.J., Lee, K.C., Han, S.J., Bui, D.A., Davidson, M., Mogilner, A., Danuser, G., 2015. Competition for actin between two distinct F-actin networks defines a bistable switch for cell polarization. Nat. Cell Biol. 17 (11), 1435–1445.
Macklin, P., Lowengrub, J.S., 2008. A new ghost cell/level set method for moving boundary problems: application to tumor growth. J. Sci. Comput. 35 (2–3), 266–299.
Maity, D., Bera, K., Li, Y., Ge, Z., Ni, Q., Konstantopoulos, K., Sun, S.X., 2022. Extracellular hydraulic resistance enhances cell migration. Adv. Sci. 9 (29), 2200927.
Maity, D., Li, Y., Chen, Y., Sun, S.X., 2019. Response of collagen matrices under pressure and hydraulic resistance in hydrogels. Soft Matter 15, 2617–2626.
Mattila, P.K., Lappalainen, P., 2008. Filopodia: molecular architecture and cellular functions. Nat. Rev. Mol. Cell Biol. 9 (6), 446–454.
Medalia, O., Beck, M., Ecke, M., Weber, I., Neujahr, R., Baumeister, W., Gerisch, G., 2007. Organization of actin networks in intact filopodia. Curr. Biol. 17 (1), 79–84.
Mittal, R., Iaccarino, G., 2005. Immersed boundary methods. Annu. Rev. Fluid Mech. 37, 239–261.
Montell, D.J., Yoon, W.H., Starz-Gaiano, M., 2012. Group choreography: mechanisms orchestrating the collective movement of border cells. Nat. Rev. Mol. Cell Biol. 13 (10), 631–645.
Mori, Y., Jilkine, A., Edelstein-Keshet, L., 2008. Wave-pinning and cell polarity from a bistable reaction–diffusion system. Biophys. J. 94 (9), 3684–3697.
Mori, Y., Peskin, C.S., 2008. Implicit second-order immersed boundary methods with boundary mass. Comput. Methods Appl. Mech. Engrg. 197 (25–28), 2049–2067.
Moure, A., Gomez, H., 2021. Phase-field modeling of individual and collective cell migration. Arch. Comput. Methods Eng. 28, 311–344.
Paul, C.D., Mistriotis, P., Konstantopoulos, K., 2017. Cancer cell motility: lessons from migration in confined spaces. Nat. Rev. Cancer 17 (2), 131.
Peskin, C.S., 2002. The immersed boundary method. Acta Numer. 11, 479–517.
Petrie, R.J., Koo, H., Yamada, K.M., 2014. Generation of compartmentalized pressure by a nuclear piston governs cell motility in a 3D matrix. Science 345 (6200), 1062–1065.
Pollard, T.D., Blanchoin, L., Mullins, R.D., 2000. Molecular mechanisms controlling actin filament dynamics in nonmuscle cells. Annu. Rev. Biophys. Biomol. Struct. 29 (1), 545–576.
Pollard, T.D., Borisy, G.G., 2003. Cellular motility driven by assembly and disassembly of actin filaments. Cell 112 (4), 453–465.
Pollard, T.D., Cooper, J.A., 2009. Actin, a central player in cell shape and movement. Science 326 (5957), 1208–1212.
Rappel, W.-J., Edelstein-Keshet, L., 2017. Mechanisms of cell polarization. Curr. Opin. Syst. Biol. 3, 43–53.
Rejniak, K.A., 2007. An immersed boundary framework for modelling the growth of individual cells: an application to the early tumour development. J. Theoret. Biol. 247 (1), 186–204.
Saad, Y., Schultz, M.H., 1986. GMRES: A generalized minimal residual algorithm for solving nonsymmetric linear systems. SIAM J. Sci. Comput. 7 (3), 856–869.
Shao, D., Levine, H., Rappel, W.-J., 2012. Coupling actin flow, adhesion, and morphology in a computational cell motility model. Proc. Natl. Acad. Sci. 109 (18), 6851–6856.
Stricker, J., Falzone, T., Gardel, M.L., 2010. Mechanics of the F-actin cytoskeleton. J. Biomech. 43 (1), 9–14.
van der Woude, L.L., Gorris, M.A.J., Halilovic, A., Figdor, C.G., de Vries, I.J.M., 2017. Migrating into the tumor: a roadmap for T cells. Trends Cancer 3 (11), 797–808.
Vitriol, E.A., McMillen, L.M., Kapustina, M., Gomez, S.M., Vavylonis, D., Zheng, J.Q., 2015. Two functionally distinct sources of actin monomers supply the leading edge of lamellipodia. Cell Rep. 11 (3), 433–445.

Wei, C., Wang, X., Chen, M., Ouyang, K., Song, L.-S., Cheng, H., 2009. Calcium flickers steer cell migration. Nature 457 (7231), 901–905.

Wolf, K., Alexander, S., Schacht, V., Coussens, L.M., von Andrian, U.H., van Rheenen, J., Deryugina, E., Friedl, P., 2009. Collagen-based cell migration models *in vitro* and *in vivo*. In: Seminars in Cell & Developmental Biology, vol. 20. Elsevier.

Wolgemuth, C.W., Zajac, M., 2010. The moving boundary node method: A level set-based, finite volume algorithm with applications to cell motility. J. Comput. Phys. 229, 7287–7308.

Yao, L., Li, Y., 2022. Effective force generation during mammalian cell migration under different molecular and physical mechanisms. Front. Cell Dev. Biol. 10, 903234.

Yao, L., Mori, Y., 2017. A numerical method for osmotic water flow and solute diffusion with deformable membrane boundaries in two spatial dimension. J. Comput. Phys. 350, 728–746.

Yao, L., Mori, Y., Sun, S.X., Li, Y., 2023. On the role of myosin-induced actin depolymerization during cell migration. Mol. Biol. Cell 34 (6), ar62.

Zhang, Y., Li, Y., Thompson, K.N., Stoletov, K., Yuan, Q., Bera, K., Lee, S.J., Zhao, R., Kiepas, A., Wang, Y., Mistriotis, P., Serra, S.A., Lewis, J.D., Valverde, M.A., Martin, S.S., Sun, S.X., Konstantopoulos, K., 2022. Polarized NHE1 and SWELL1 regulate migration direction, efficiency and metastasis. Nature Commun. 13, 6128.